



funded by the European Union

---

# Awareness and resilience through European multi sensor system

---

## D4.1 Report of the monitoring data of the test sites hydrogeological parameters

Version 1

## Disclaimer

Funded by the European Union. Views and opinions expressed are however those of the author(s) only and do not necessarily reflect those of the European Union or of the European Commission-Euratom. Neither the European Union nor the granting authority can be held responsible for them.

While this document has been prepared with care, the authors and their employers provide no warranty concerning the content and shall not be liable for any direct, incidental or consequential damages that may result from the use of the information or the data contained in it. Reproduction is authorised provided the material is unabridged and the source is acknowledged.

Document type	Deliverable
Document number	D4.1 Version 1
Document title	Report of the monitoring data of the test sites hydrogeological parameters
Authors	Vasileios Anagnostou, Torbjörn Bäck, Pavlos Bonatis, Gaetano De Luca, Jurgen Gerl, Vincenzo Guerriero, Kumar Gururaj, Vasileios Karakostas, Christos Kourouklas, Mats Nilson, Gregory Nuel, Ayse Nyberg, Eleftheria Papadimitriou, Peter Sjödin, Stelios Stoulos, Marco Tallini, Patryk Törngren
Release date	30/08/2024
Contributing partners	AuTh, ETH, GSI, INGV, KTH, SU, UNIVAQ
Dissemination level	Public

Version	Short description	Main author	Coordinator
1	First Release	Vasileios Anagnostou (AuTh) Torbjörn Bäck (KTH) Pavlos Bonatis (AuTh) Gaetano De Luca (INGV) Jurgen Gerl (GSI) Vincenzo Guerriero (UNIVAQ) Gururaj Kumar (KTH) Vasileios Karakostas (AuTh) Christos Kourouklas (AuTh) Mats Nilson (KTH) Gregory Nuel (SU) Ayse Nyberg (KTH) Eleftheria Papadimitriou (AuTh) Stelios Stoulos (AuTh) Peter Sjödin (KTH) Marco Tallini (UNIVAQ) Patryk Törngren (KTH)	Ayse Nyberg, KTH

## Abstract

The present D4.1 deliverable pertains to the description of the installation procedure of the first six (6) prototype sensors of the artEmis project in the chosen areas (Abruzzo region, Italy; Lefkada Islands, Greece; Bedretto lab and Swiss Alps, Switzerland). The Abruzzo region (Italy) has been managed mainly by UNIVAQ and INGV, the Ionian islands and the Gulf of Corinth (Greece) by AUTH, and Bedretto lab and Swiss Alps by ETH. The installation procedure concerning both technical, communication and data transmission issues was implemented with the continuous cooperation and collaboration of KTH, GSI and SU.

Deliverable D4.1 discuss in brief the description of the geological, hydrogeological and seismotectonic setting of the installation sites, while describing in detail the on-field workflow of the installation, including information about the installation plan and management, the details regarding (i) the power supply, (ii) the verification of functionality of the six sensor prototypes, (iii) their communication accessibility and (iv) the data transmission testing.

## Table of contents

Disclaimer .....	2
Abstract .....	4
Table of contents.....	5
1 Introduction.....	6
1.1 References.....	6
2 Monitoring the hydrogeological parameters in the Ionian Island and Corinth Gulf (Greece).....	7
2.1 Sensors Installation Sites.....	7
2.1.1 Brunello Installation Site .....	9
2.1.2 Komilio Installation Site .....	13
2.2 Monitoring and operation of the installed sensors .....	16
2.3 Seismicity evolution during the target period .....	20
2.4 Monitoring of the hydrogeological parameters during the target period.....	23
2.5 References.....	27
3 Monitoring the hydrogeological parameters in the Abruzzi region (Italy) .....	27
3.1 Sensors Installation Sites.....	27
3.1.1 Gran Sasso groundwater intake tunnels- sites 2 and 3 .....	27
3.1.2 Gran Sasso groundwater intake tunnels- sites 2 and 3 .....	35
3.2 Monitoring and operation of the installed sensors .....	38
3.3 Monitoring of the hydrogeological parameters during the target period.....	43
3.4 References.....	51
4 Monitoring the hydrogeological parameters in the Swiss Alps and Bedretto Lab .....	51
4.1 Sensors Installation Sites.....	51
4.2 Monitoring and operation of the installed sensors .....	52
4.3 Seismicity evolution during the target period .....	54
4.4 Geochemical evolution during the target period.....	56
4.5 References.....	59

## 1 Introduction

The present report is associated with the D4.1 deliverable of the artEmis project entitled “*Report of the monitoring data of the test sites hydrogeological parameters (Abruzzi region, Swiss Alps, Ionian Islands and Gulf of Corinth)*”. It includes the installation of the prototype sensors in Greece (two (2) sensors), Italy (three (3) sensors) and Switzerland (one (1) sensor), the ongoing seismicity and the temporal variation of the meteorological & hydrological parameters, during the February – August 2024 time interval.

Regarding the scope of the artEmis project (<http://www.artemisproject.eu/>), a multiparametric advanced and low-coast sensors network will monitor radon in groundwater. The network is designed to be of a high spatial density in selected study areas in Greece, Italy and Switzerland.

The selection of the sites for radon monitoring was based on several criteria for ensuring a robust assessment of radon levels. The process involved investigation of the soil and bedrock composition, the soil permeability and most importantly the proximity of seismic faults and strong earthquake locations. The installation of the sensors near active faults might result in clearer detection of remarkable radon fluctuations because earthquake preparatory processes it facilitates or inhibit migration paths for radon gas from deeper crustal layers. The sites’ accessibility is also an important factor for regular monitoring and maintenance of the equipment. The chosen locations will provide a representative, reliable and comprehensive observational database for promoting our understanding of radon emanation and its relationship with active crustal deformation and seismogenesis.

The radon content in underground waters (waters from wells that are some meters deep and springs along active fault lines) is one of the important forerunners of earthquake activity (Kawabata et al., 2020 and references therein; Morales-Simfors et al., 2020 and references therein). Along with water levelling (water discharge) and water temperature, might present anomalous behavior in periods ranging from a few days to several months before and after earthquake activity. Meteorological parameters such as temperature, pressure, humidity, wind velocity, and precipitation, significantly affect radon emissions and concentration levels. Understanding how these variations are crucial, leads to more accurate radon monitoring and assessment.

Changes in atmospheric pressure, for example, can affect radon levels, as low atmospheric pressure can enhance radon exhalation and conversely, high pressure may suppress radon release. Rainfall can also influence radon emissions in various ways. Heavy rain can temporarily seal the soil surface, trapping radon gas and reducing its exhalation. However, after the rain, when the soil dries, radon emissions may increase as the trapped gas is released. Snow cover acts as a barrier that prevents radon from escaping the soil. During winter, the accumulation of snow can lead to higher radon levels, which may be released rapidly during melting (Stoulos et al, 2024 and references therein).

The integration of the observations during the process of radon monitoring and interpretation will enhance our understanding of the physical mechanisms governing the association of seismogenesis with radon emission, contributing to more effective mitigation strategies.

### 1.1 References

Kawabata, K., Sato, T., Takahashi, H. A., Tsunomori, F., Hosono, T., Takahashi, M., Kitamura, Y., 2020. Changes in groundwater radon concentrations caused by the 2016 Kumamoto earthquake. *Journal of Hydrology* 584, 124712. <https://doi.org/10.1016/j.jhydrol.2020.124712>

Morales-Simfors, N., Wyss, R. A., Bundschuh, J., 2020. Recent progress in radon-based monitoring as seismic and volcanic precursor: A critical review. *Critical reviews in environmental science and technology* 50(10), 979-1012. <https://doi.org/10.1080/10643389.2019.1642833>

Stoulos, S., Papadimitriou, E., Karakostas, V., Kourouklas, Ch., Atac-Nyberg, A., Wyss, R., Bäck, T., Tallini, M., DeLuca, G., 2024. Radon signals in soil gas associated with earthquake occurrence in Greece: review and perspective. *Journal of Radioanalytical and Nuclear Chemistry* (accepted).

## 2 Monitoring the hydrogeological parameters in the Ionian Island and Corinth Gulf (Greece)

### 2.1 Sensors Installation Sites

The selection of the installation sites of the first two prototype sensors in Lefkada Island has been made upon consideration of its geological and hydrolithological setting, the seismotectonic properties and seismic activity, given that radon release in groundwater depends on these factors (e.g., Kawabata et al., 2020). Additionally, the logistics of the selected sites, namely the power supply availability and the internet network coverage, were also taken into account for the installation. The two prototype sensors were installed in open wells—one in the seaside area of Agios Ioannis (Brunello), approximately 3.5 km west of Lefkada city, and the other at the entrance of Komilio village, about 17 km SSW of Lefkada city. Both installation sites (red triangles in map of Figure 2.1) are very close to the major right-lateral strike slip faults located along the western coasts of the Island (red solid lines in map of Figure 2.1).

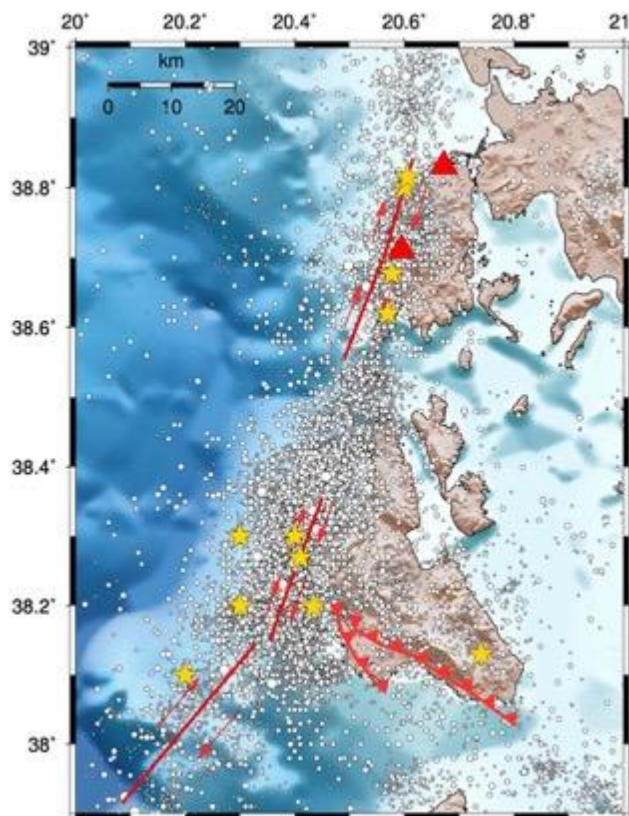


Figure 2.1: Epicentral distribution of  $M \geq 2.0$  earthquakes occurred in central Ionian Islands since 2003 (tiny, small, moderate and large white circles depict the  $2.0 \leq M < 3.0$ ,  $3.0 \leq M < 4.0$ ,  $4.0 \leq M < 5.0$  and  $5.0 \leq M < 6.0$  earthquakes, respectively). Yellow stars depict the  $M \geq 6.0$  occurred since 1948. Red solid lines depict the major fault segments, that were activated in the area during the last five decades, and the antiparallel red arrows represent the right-lateral strike slip motion. Red triangles denote the installation sites, Brunello at the northern and Komilio at the southern point.

The first installation site, Brunello, in Agios Ioannis area west of the city of Lefkada, is located about 5 km east from the northern tip of Lefkada North fault segment and 17.6 km NNE from the southern tip of this segment (Figure 2.1). Brunello is located 17.8 km and 34.5 km NNE from the northern and southern tips of Lefkada South fault segment, respectively. The distances of the installation site from the epicenters of the four  $M > 6.0$  earthquakes which occurred in Lefkada Island since 1948 (Table 2.1) reports values ranging from 6 km (distance from the 2003  $M = 6.2$  earthquake) up to 25 km (distance from the epicenter of the 22<sup>th</sup> April 1948  $M = 6.5$  main shock).

The location of the second installation site in Lefkada Island is shown in Figure 2.1 by the southernmost red triangle and is in Komilio village in the central and western part of the Island. The site is located very close to both the southern tip of North Lefkada fault segment associated with the 2003  $M_w$  6.2 main shock (3 km) and the northern tip of South Lefkada fault segment associated with the 2015  $M_w$  6.5 main shock (3.4 km). The distances from the northern tip of North Lefkada fault segment and from the southern tip of South Lefkada fault segment are equal to 14.5 km and 19.6 km, respectively (Table 2.2). The distances of the Komilio installation site from the epicenters of the four  $M > 6.0$  earthquakes that occurred in Lefkada Island since 1948 (Table 2.2) range from 4.1 km (2015  $M = 6.5$ ) up to 10.5 km (first main shock of 1948 with  $M = 6.5$ ). Overall, the epicenters of all the four large ( $M > 6.0$ ) main shocks since 1948 are located at distances inside a radius of  $\sim 12$  km around the Komilio installation site.

Installation Site	Distance from:	Distance (km)
Brunello (38.831/ 20.672)	North tip of Lefkada North Fault Segment	5
	South tip of Lefkada North Fault Segment	17.6
	North tip of Lefkada South Fault Segment	17.8
	South tip of Lefkada South Fault Segment	34.5
	1948 04 22 $M = 6.5$ earthquake epicenter	25
	1948 06 30 $M = 6.4$ earthquake epicenter	7.1
	2003 $M = 6.2$ earthquake epicenter	6
	2015 $M = 6.5$ earthquake epicenter	19

Table 2.1 Distances (in km) of Brunello installation site from the Lefkada North and South fault segments and from the epicenters of the four  $M > 6.0$  earthquakes that occurred in Lefkada Island since 1948.

Installation Site	Distance from:	Distance (km)
Komilio (38.711/ 20.595)	North tip of Lefkada North Fault Segment	14.5
	South tip of Lefkada North Fault Segment	3
	North tip of Lefkada South Fault Segment	3.4
	South tip of Lefkada South Fault Segment	19.6
	1948 04 22 $M = 6.5$ earthquake epicenter	10.4
	1948 06 30 $M = 6.4$ earthquake epicenter	9.9
	2003 $M = 6.2$ earthquake epicenter	11.6
	2015 $M = 6.5$ earthquake epicenter	4.1

Table 2.2 Distances (in km) of Komilio installation site from the Lefkada North and South fault segments and from the epicenters of the four  $M > 6.0$  earthquakes that occurred in Lefkada Island since 1948.

Moving to the criteria based on the geological setting of the installation sites, Brunello (Agios Ioannis area; the northern red triangle in the map of Figure 2.2) is located upon the intersection of the medium porosity Quaternary and Plio-Pleistocene granular sediments (yellow colored formations in Figure 2.2), medium-high porosity Cretaceous limestones and dolomites and varying in permeability Jurassic–Cretaceous thick-bedded limestones (blue colored formations in Figure 2.2). The aforementioned geological formations are capable for the sensors' installation due to their intermediate to high permeability allowing the groundwater aquifers to be recharged. On the other hand, the Komilio site is located upon flysch formations (dark brown colored formations in Figure 2.2). Although flysch is a low porosity formation is also capable for sensors installation under specific conditions, when it is associated with a fractured aquifer in undrained conditions near active faults, as Kuo et al. (2020) suggests, which is also the case for the selected site.

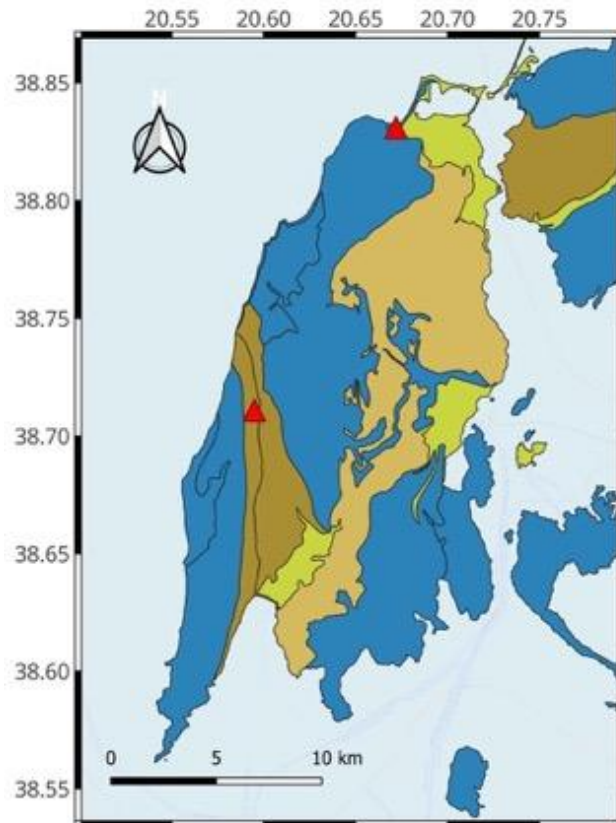


Figure 2.2: Simplified geological map of Lefkada Island in which the medium porosity Quaternary and Plio-Pleistocene granular sediments are depicted in yellow and light brown colors, respectively. The medium-high porosity Cretaceous limestones and dolomites and Jurassic–Cretaceous thick-bedded limestones are depicted in blue, and the flysch formation is depicted in dark brown. The installation sites are shown by the red triangles, Brunello (Agios Ioannis) at the northern and Komilio at the southern point.

### 2.1.1 Brunello Installation Site

The prototype sensor (System Number 4) was installed at the private ground of Brunello Hotel, west of Lefkada city (Agios Ioannis area; Figures 2.3 and Figure 2.4). The installation site is a traditional open water well (Figure 2.5), with a varying depth between 2 m and 3 m (Figure 2.6). Inside the well pre-exists a water pumping system with electrical connection, which is no longer used. Installation was carried out on 13 February 2024, with an installation time of 3.5 hours. The installed system includes the sensor, transmitter and base station (gateway) units. The sensor unit consists of the Scionix detector no. 3 - Sensor unit S003 V3.1, V2 with an additional external pressure sensor. Sensor unit was fixed with cable binders upon an iron cage like structure with a grey-colored rod, being manufactured for the installation needs (Figure 2.7). For

further support of the sensor sinking into the water a floater system from a styrodur block 16x15x10 cm<sup>3</sup> was used, for keeping dangling system with the sensor at constant depth of approximately 50 cm below the water surface (Figure 2.8). Ethernet cable of sensor unit fixed with cable binders to a rope. The rope is loosely hanging to allow for water level variation of approximately 1 m, to avoid submersion of the ethernet cable.



Figure 2.3: Installation site of the Brunello Station (System Number 4).



Figure 2.4: Installation site of the Brunello Station (System Number 4), in which the installation well is enclosed by the red rectangle.



Figure 2.5: The installation well of the Brunello Station (System Number 4).

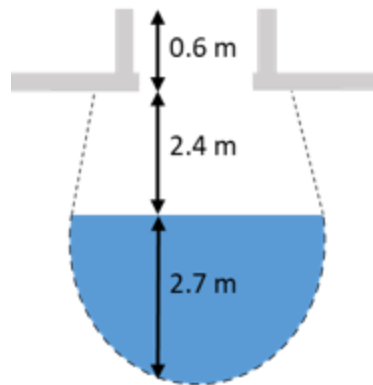


Figure 2.6: Schematic representation of the Brunello Station (System Number 4) installation well, shown in vertical cross section.



Figure 2.7: The Scionix detector no. 3 - Sensor unit S003 V3.1 and the dangling system for supporting the sensor.



Figure 2.8: Sinking the sensor along with a floating buoy to keep the pending rope under the water level and the sensor inside the water.

The transmitter unit (T004 V3) screwed inside the concrete rim of the well (Figure 2.9) and it was tuned to 5.1V. The ethernet cable from the transmitter unit to the gateway one was led through a hole in the rim. For most of its length (30m), the cable was kept inside the well, mounted on its wall (Figure 2.9). The base station unit consists of the Gateway system no. 7 with internal 12V and 5V supplies connected to an available AC outlet. It was screwed from outside to the concrete rim and was powered an AC outlet on the rim. A Greek SIM card is installed in a D-link router, providing 4G mobile network to the system. It is supplied by USB from Gateway and kept inside the gateway system box for protection purposes.



Figure 2.9: Transmitter unit of Brunello Station, as it was mounted onto the walls of the well.



Figure 2.10: The gateway unit (denoted inside the red circle) and the D-link router (denoted by the light blue circle) used for the installation of Brunello Station.

### 2.1.2 Komilio Installation Site

The second prototype sensor (System Number 5) was installed on a public traditional open well, occasionally used for irrigation, at the entrance of Komilio village (Figures 2.11 and 2.12), with its depth to be approximately equal to 7.5 m (Figure 2.13). Inside the well pre-exists a water pumping system with electrical connections and tubing left inside the well for occasional use. Installation was carried out on 15 February 2024, with an installation time of 2 hours. The installed system includes the sensor, transmitter and base station (gateway) units. The sensor unit consists of the Csl (TI) detector no. 3 - Sensor unit S006 V3.1, V2 without external pressure sensor. Similarly to the Brunello Station, the sensor unit was fixed with cable binders upon an iron cage-like structure with a grey-colored rod, being manufactured for the installation needs (Figure 2.14). For further support of the sensor sinking into the water, a floater system from styrodur block 2x16x10 cm<sup>3</sup> was used, for keeping the dangling system with the sensor at a constant depth of approximately 50 cm below the water surface (Figure 2.15). The ethernet cable of the sensor unit was fixed with cable binders to a rope. The length of the cable was equal to 6.5 m. The rope is loosely hanging to allow for water level variation of approximately -1/+5 m.



Figure 2.11: Installation site of the Komilio Station (System Number 5).



Figure 2.12: The installation well of the Komilio Station (System Number 5).

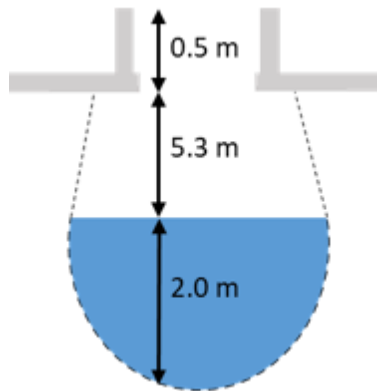


Figure 2.13: Schematic representation of the Komilio Station (System Number 5) installation well, shown in vertical cross section.



Figure 2.14: The CsI (TI) detector no. 3 - Sensor unit S006 and the dangling system used for supporting the sensor.

The transmitter unit (T005 V3) was screwed inside the concrete rim of the well (Figure 2.15) and it was tuned to 5.1V. The ethernet cable from the transmitter unit to the gateway one was led through a hole in the rim. For most of its length (30m), the cable was kept inside the well, mounted on its wall (Figure 2.15). The base station unit consists of the Gateway system no. 6 with internal 12V and 5V supplies connected to an available AC outlet. It was screwed from outside to the concrete wall close to the power distributor and was powered by an AC outlet in the distributor (Figure 2.16). A Greek SIM card is installed in a D-link router, providing 4G mobile network to the system. It is supplied by USB from gateway and kept inside gateway system box for protection purposes.



Figure 2.15: Transmitter unit of Komilio Station, as it was mounted onto the walls of the well.



Figure 2.16: Gateway (base) unit of Komilio Station, as it was mounted onto the walls of the well (red rectangle), and the power supply system of installation site.

## 2.2 Monitoring and operation of the installed sensors

Once the 2 prototype sensors (Brunello and Komilio Stations) were successfully installed, their communication functionality was verified and their transmission status to the cloud database was tested. Table 2.3 presents the site considerations for the installation sites in Lefkada Island. On-site performed test showed that the sensors and the full chain communication system properly worked. Tables 2.4 and 2.5 summarise the obtained reports of the sensors' prototypes installed in Brunello and Komilio sites.

System No.	Site No.	Site name	Type	Wifi / mobile	Distance		Comments
					Sensor – transm.	transm. – gateway	
4	1	Brunello (Agios Ioannis)	Open Well	Mobile	5 m 1 m (kept 30 m)		Deep, varies by 2 – 3 m
5	2	Komilio	Open Well	Both	6.5 m 10 m (kept 30 m)		Deep, varies considerably

Table 2.3: Site considerations for the two sensor prototypes installed in Lefkada Island, Greece.

Sensor Parameter	Reported Status / Value
Gamma count rate	7 counts per second in all channels (500 channels)
Pressure inside the casing	1013.47 hPa
Temperature	22.79 C
Humidity	49.59%
Sensor level above sea	-1.85m
Microphone value	854 (noise level)
Peak position shifting	No
Histogram Scale	1

Table 2.4: Report of the sensor prototype installed in Brunello Station (System Number 4).

Sensor Parameter	Reported Status / Value
Gamma count rate	3 count per second in all channels (500 channels)
Pressure inside the casing	957.96 hPa
Temperature	20.57 C
Humidity	66.20%
Sensor level above sea	470.77m
Microphone value	848 (noise level)
Peak position shifting	No
Histogram Scale	5

Table 2.5: Report of the sensor prototype installed in Komilio Station (System Number 5).

The sensors were tested using a Cs-137 radioactive source before being installed in the field. The spectrum collected is illustrated in the following figure (Figure 2.17).

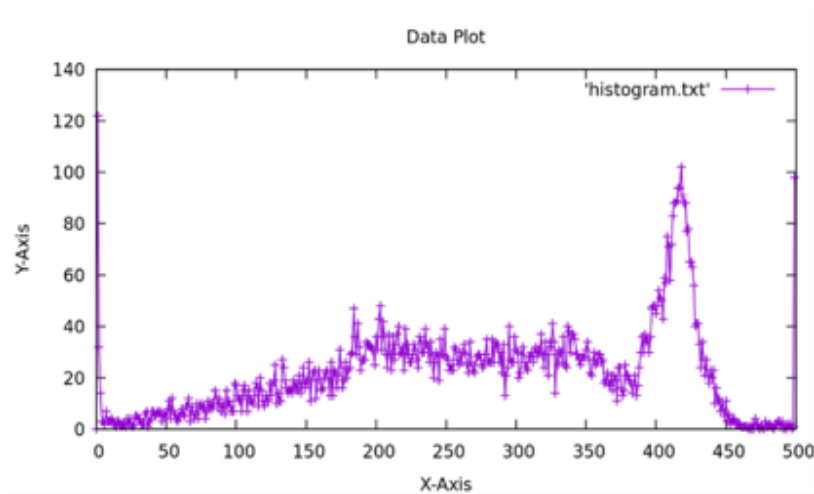


Figure 2.17: Spectrum collected before the sensor's installation using a Cs-137 radioactive source.

The spectrum is not energy calibrated, so the horizontal axis (x-axis) is expressed in channel and not in keV. Each channel is a voltage bin (x-axis), and all the signals collected by the detector that have a pulse high between the specific voltage bin are measured as counts in that bin (y-axis). The peak of Cs-137 with energy 662 keV appeared in the ~420 channel. Any lower signal accumulates in lower channels.

After the installation of the Brunello and Komilio stations the gamma spectrum was measured. In Brunello, the sensor was at 1.85 m below sea level and recorded 1013.47 hPa pressure, a temperature of 22.79 C and 49.59% humidity. The count rate (cps) was 7 counts per second, integrating the entire spectrum of 500 channels, as illustrated below (Figure 2.18).

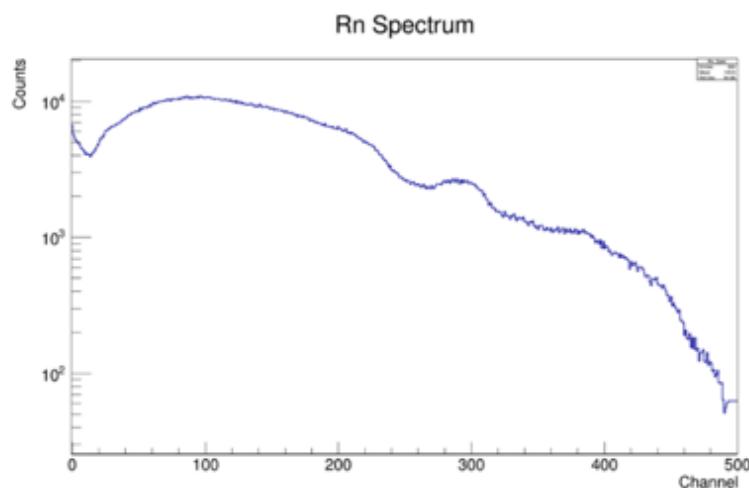


Figure 2.18: Example of gamma spectrum measures at Brunello Station.

The spectrum showed a peak of 609 keV at 300 channels, which corresponds to Bi-214, a radon progeny. The area between channels 50 and 250 is the backscattered photons from the sensor surroundings.

In Komilio, the sensor was 470 m above sea level and recorded 957.96 hPa pressure, a temperature of 20.57 C, and 66.20 % humidity. The count rate (cps) was 3 counts per second, integrating the entire spectrum of 500 channels, as illustrated in the next figure (Figure 2.19).

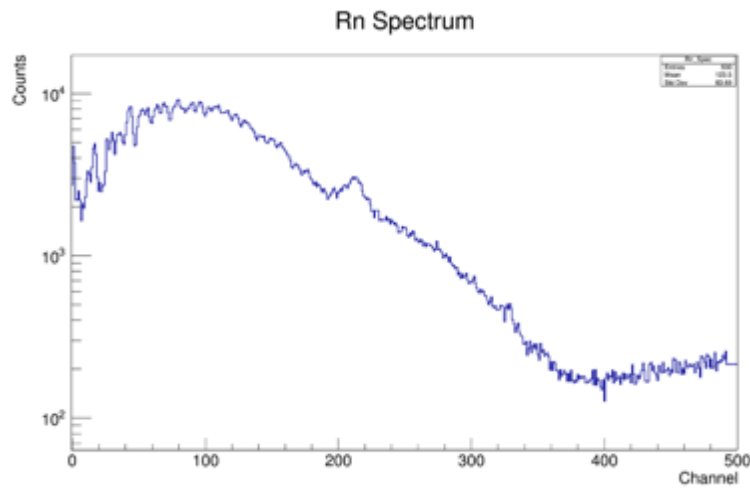


Figure 2.19: Example of gamma spectrum measures at Komilio Station.

Similarly to Brunello, the 609 keV peak now appears in the 220 channels. The count rate is now 3 counts per sec (cps) instead of 7 cps in Brunello, which means that the Rn level (Bq m<sup>-3</sup>) in Komilio is more than half that in Brunello.

Figure 2.20 presents the raw spectra measured on August 11th (blue line) and 12th (red line), 2024. The spectra are identical and show no variation during the two-day measurement.

The spectrum should be energy-calibrated, so each channel should correspond to a specific energy. The sensor's calibration curve is presented in the next Figure (Figure 2.21).

The curve is not linear but parabolic, so the energies below 700 keV are measured with high accuracy while the higher energies are barely detected. Based on the above calibration curve, the raw data measured in Komilio are now expressed in KeV instead of channel, as illustrated in the following Figure (2.22).

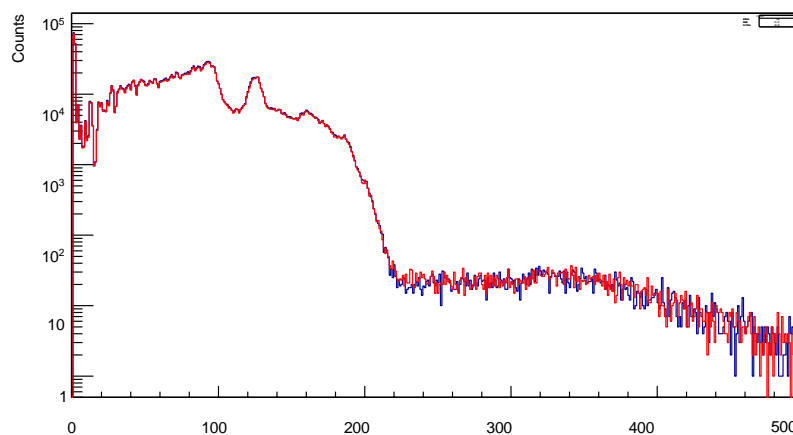


Figure 2.20: Raw spectra measured on 11<sup>th</sup> (blue line) and 12<sup>th</sup> (red line) August 2024 on Komilio Station.

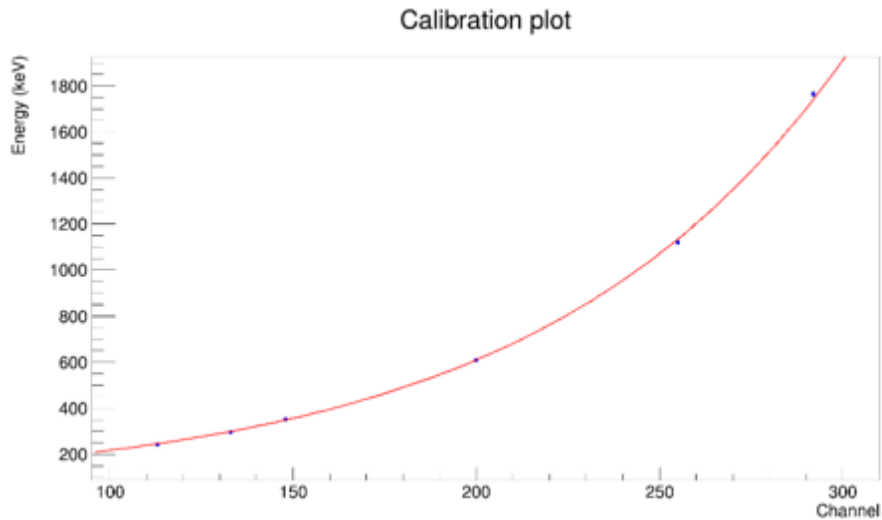


Figure 2.21: Calibration curve of Komilio Station.

### Calibrated Energy Spectrum

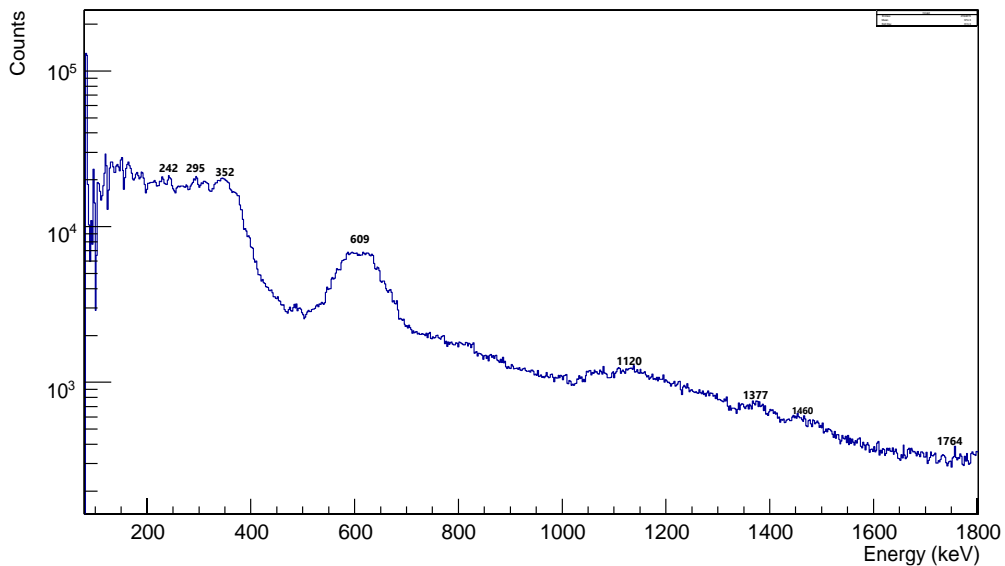


Figure 2.22: The energy of the gamma rays detected by the sensor at Komilio Station.

The Rn daughter gamma rays dominate the spectrum, with the 609 keV peak of Bi-214 having excellent resolution and giving reliable data on the Rn variations in the groundwater. Also, the 1120 keV, 1377 keV, and 1764 keV peaks of Bi-214 and the 242 keV, 295 keV, and 351 keV of Pb-214 were detected with poor resolution.

Since the sensor barely detected the 1460 KeV peak of K-40, it is not possible to detect any other gamma rays from any isotope above Rn and Tn, like 911 keV. In the case of Th-progenies the 238 keV peak of Pb-212 was also detected. The peak at 242 keV comes from the combination of the following gamma rays: 239 keV of Pb-212 (43.3%) plus 242 keV of Pb-214 (7.4 %). The intensity of the gamma rays demonstrates that the peak is mostly due to Th-series measuring counts that, in principle, originated from Thoron progeny of Pb-212. The gamma rays of K-40 (1461 keV) and the Tn daughter of Pb-212 (238 keV) are also detected with poor resolution.

### 2.3 Seismicity evolution during the target period

The AUTH team has been consistently and thoroughly studying the seismicity evolution in the central Ionian Islands region of western Greece within the artEmis project framework. Since the 2003 Lefkada ( $M_w = 6.3$ ) earthquake and the installation of a local seismic network for its detailed study (Karakostas et al., 2004), continuous seismic monitoring in the area of the central Ionian Islands has been substantially enhanced. The local seismological network (2007-today) operated by the Geophysics Department of the Aristotle University of Thessaloniki (GD-AUTH) in collaboration with the Regional Union of Municipalities of Ionian Islands (PED-IN), which is a local partner of artEmis project, has significantly contributed to this direction. Nowadays, the dense permanent network of seismic stations, part of the Hellenic Unified Seismic Network (HUSN) provides high-quality waveform data and contributes to the improved understanding of the intricate seismotectonic properties of the region.

Over the past five months since the installation of the Brunello and Komilio sensors, seismic activity has taken place in the broader area of Western Greece (Figure 2.23). In distances less than 150km from the reference point at the central Ionian Islands installed sensors, over 1000 earthquakes with magnitudes  $M \geq 1.5$  occurred. During this period, five moderately strong earthquakes ( $4.0 \leq M < 5.0$ ) were recorded, four of which occurred on the mainland of Greece, while one was located on Kefalonia Island (Table 2.6). The majority of the seismic activity occurred in the offshore area west of Asos village in the northern part of Kefalonia Island and was thoroughly studied over a two-month span, from February to April 2024. This swarm-like activity is continued in the area, thus a discussion about the time and magnitude distribution, as well as periods of increased activity and quiescence is necessary. Isolated earthquakes with magnitudes  $3.5 \leq M < 4.0$  were also recorded in North Peloponnese, Corinth Gulf and Epirus regions of Western Greece, as well as four earthquakes in the same magnitude range that occurred offshore the central Ionian Islands, west and south of Zakynthos Island.

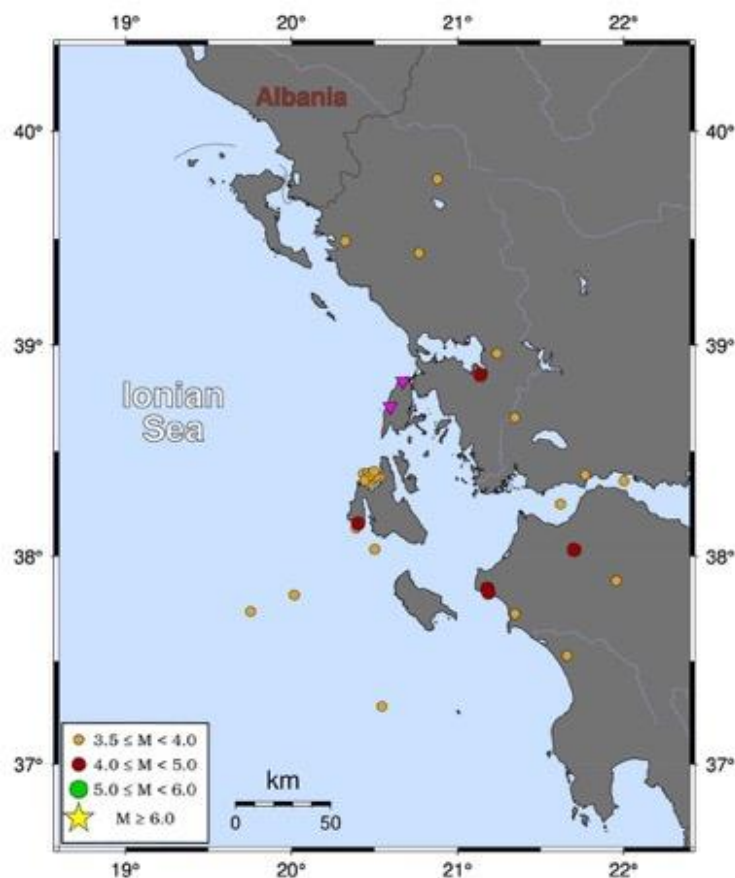


Figure 2.23: Observed seismicity ( $M \geq 3.5$ ) in Western Greece, during the approximately five-month operation of the Komilio and Brunello radon sensors (denoted by pink inverse triangles).

Date	Latitude	Longitude	Depth (km)	Magnitude
08-04-2024	38.86	21.13	13.1	4.1
10-05-2024	38.15	20.40	16.4	4.1
11-06-2024	38.03	21.70	20.1	4.3
06-07-2024	37.84	21.18	11.1	4.9
07-07-2024	37.82	21.18	6.3	4.7

Table 2.6: Epicenters, dates of occurrence and magnitude of the strongest recorded earthquakes in Western Greece, during the approximately five-month operation of Brunello and Komilio Stations.

The seismic activity in the offshore region West of Asos exhibited swarm-like characteristics, initializing and ceasing in a gradual manner, without a distinctive large earthquake (Scholz, 2019). The relocated epicenters (Figure 2.24) reveal a narrow zone striking approximately E-W, in agreement with the step-over structures that characterize the area and its stress regime (Karakostas et al., 2015).

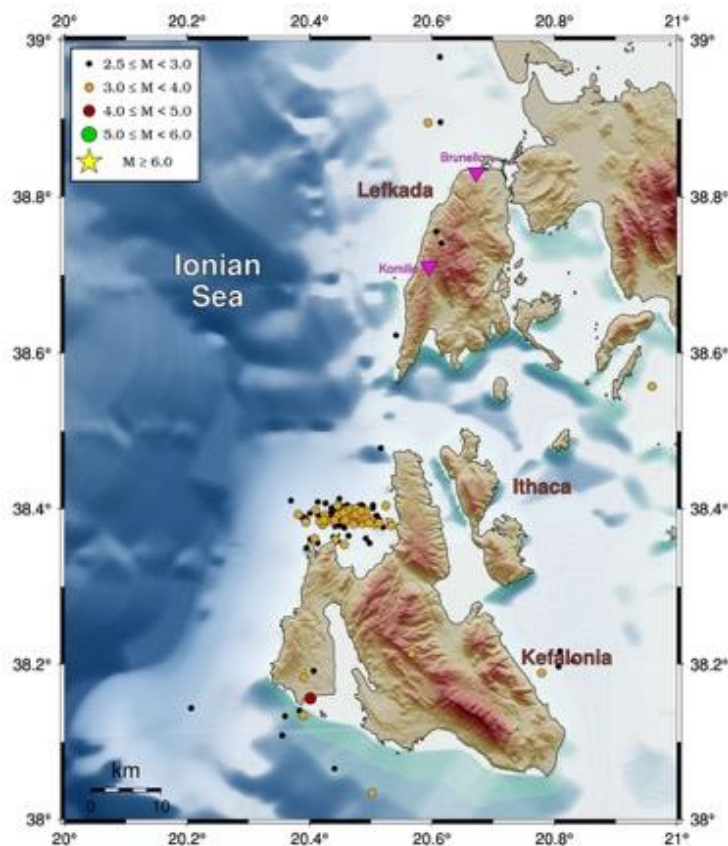


Figure 2.24: Epicentral distribution of the strongest ( $M \geq 2.5$ ) earthquakes that occurred during the swarm-like excitation of the offshore area west of Asos (Northern Kefalonia). The pink inverse triangles denote the locations of the two sensors.

The swarm-like seismic activity was initiated on February 20<sup>th</sup>, just a few days after the installation of the two sensors, with the earthquake rate peaking on March 3<sup>rd</sup>. The swarm activity in the area is continued for the whole study period and nearly 75% of the detected earthquakes since the start of radon monitoring in the region occurred during the two-month period between February and April, followed by a three-month period of relative seismic quiescence, up until July (Figure 2.25).

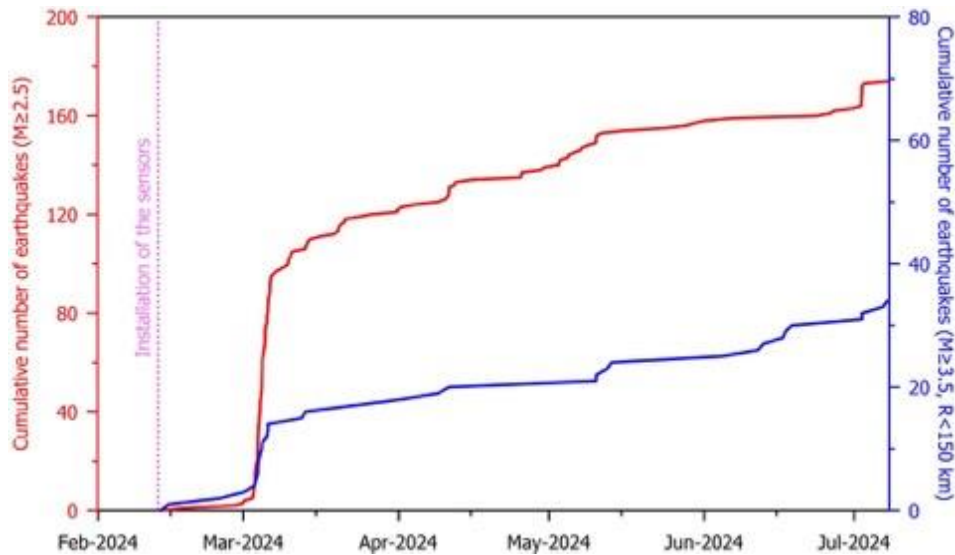


Figure 2.25: Cumulative number of earthquakes that occurred in the study area since the installation of the two radon sensors. The red line denotes earthquakes with  $M \geq 2.5$  and the blue line earthquakes with  $M \geq 3.5$  at an epicentral distance smaller than 150km from a reference point at the central Ionian Islands.

Since the majority of the earthquake activity in the study area occurred in the offshore area west of Asos village, most of the detected earthquakes up to  $M=4.0$  appear to be in an epicentral distance of approximately 40km from the Komilio sensor and 50km from the Brunello sensor. Moreover, approximately 20 moderately strong earthquakes ( $3.5 \leq M < 5.0$ ) appear to have occurred in larger epicentral distances from the two sensors, up to approximately 170km away from the sites. Lastly, few low-magnitude earthquakes ( $M < 3.0$ ) occurred relatively close to the sites ( $R < 20\text{km}$ ) (Figure 2.26).

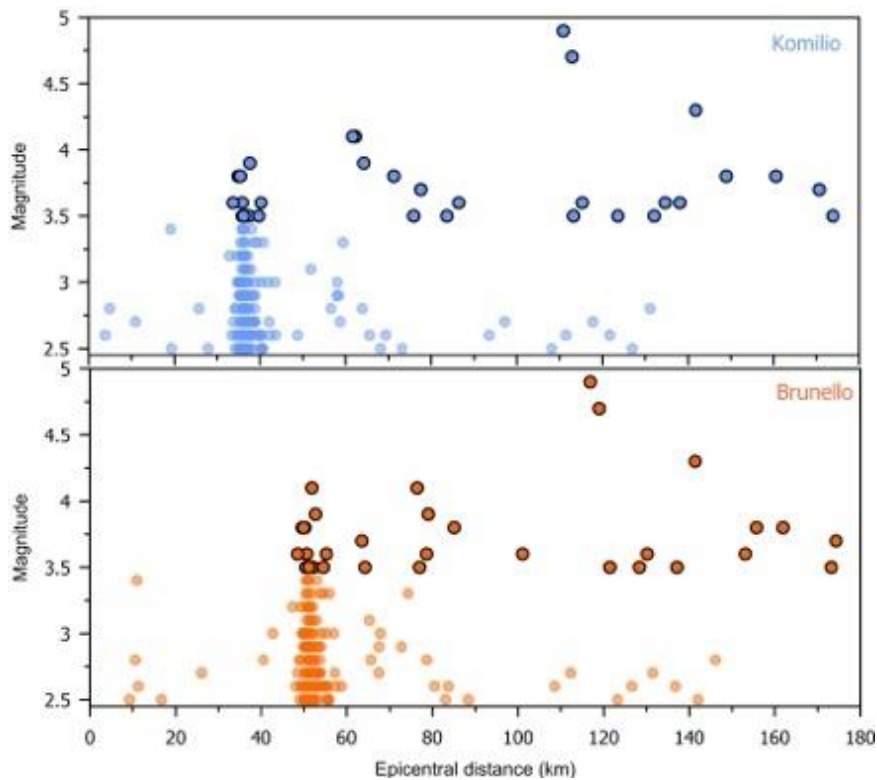


Figure 2.26: Epicentral distances of the earthquakes that occurred during the study period from the Komilio (top) and Brunello (bottom) sensors. The majority of the earthquakes occurred at approximately 40km from the Komilio site and at 50km from the Brunello site, corresponding to the activated offshore area west of Asos village (Kefalonia).

## 2.4 Monitoring of the hydrogeological parameters during the target period

Concerning the hydrogeological parameters during the target period of the present deliverable, namely from 13 February 2024 (installation date of the first prototype sensor on Lefkada Island) to 31 July 2024 the rainfall data time series were compiled. Rainfall is one of the hydrogeological parameters that strongly influences groundwater radon levels. This occurs because the barometric pressure inside the soil increases when a significant amount of rainwater enters the material's pores. Therefore, the analysis of rainfall time series, complemented by the radon signals obtained from the installed sensors, is an important step for correcting the radon signals and their potential correlations with earthquake occurrence.

The two prototype sensors were installed on Lefkada Island during 13 – 16 February 2024. As already stated, both the prototype sensors were installed into water wells, the first one (Brunello Station) in Agios Ioannis area at the northern part of the island and the second one (Komilio Station) at Komilio village at its central-western part (pink inverse triangles in map of Figure 2.27). Rainfall data for Lefkada Island is published by the National Observatory of Athens (METEO/NOA), using the monitoring of the permanent meteorological station accessible at <https://meteosearch.meteo.gr> (last accessed August 20, 2024). This station is located at the Lefkada City harbor, with an elevation of 12 meters (represented by a blue hexagon on the map in Figure 2.27). The distance from the Brunello Station (Agios Ioannis) is 3.4 km while the distance from the Komilio village sensor is 16.7 km. The proximity of the permanent meteorological station to the locations of the installed prototype sensors suggests that the rainfall recorded at the meteorological station likely had a similar effect on the sites of our interest particularly the first one in Brunello Station (Agios Ioannis).

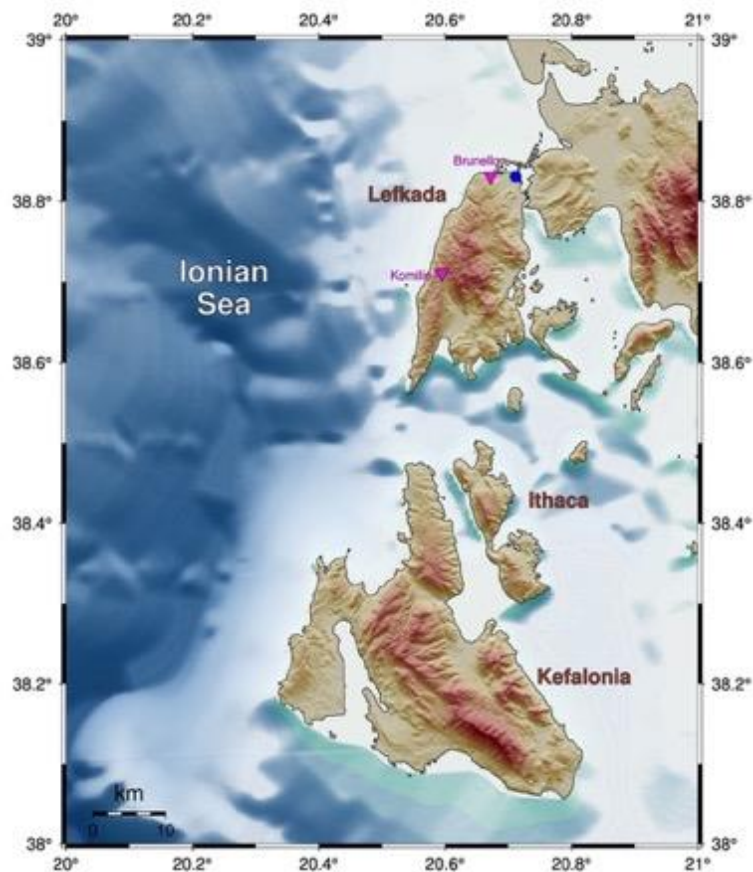


Figure 2.27: Geomorphological map of Central Ionian Islands along with the locations of the two prototype sensors installed at Lefkada Island shown as inverse triangles in pink color, whereas the location of the permanent meteorological station of Lefkada Island is depicted with the blue hexagon.

The recorded rainfall data for Lefkada Island during the target period (from February to July 2024; Figure 2.28) shows a clear trend of decreasing precipitation over the months. In February, there were two significant rainfall events, with the first occurring around February 11–12, two days before the installation of the first prototype sensor (13 February 2024; vertical red dashed line in the upper left panel of Figure 2.28), peaking above 25 mm, and a second smaller peak of 14 mm later in the same month (25 February). March experienced more frequent but less intense rainfall, with several peaks reaching around 10 mm (12.4 mm on 4 March, 10.8 mm on 11 March and 11.2 mm on 19 March). April saw a decline in rainfall frequency and intensity, with one notable peak of 19.6 mm of rainfall mid-month (19 April), and two lower peaks around 10 mm (9.2 mm and 10.0 mm on 21 and 25 April, respectively). May experienced less rainfall, with only minor peaks under 10 mm (9.6 mm and 8 mm on 4 and 14 May, respectively). Both June and July recorded no rainfall, indicating a dry summer period.

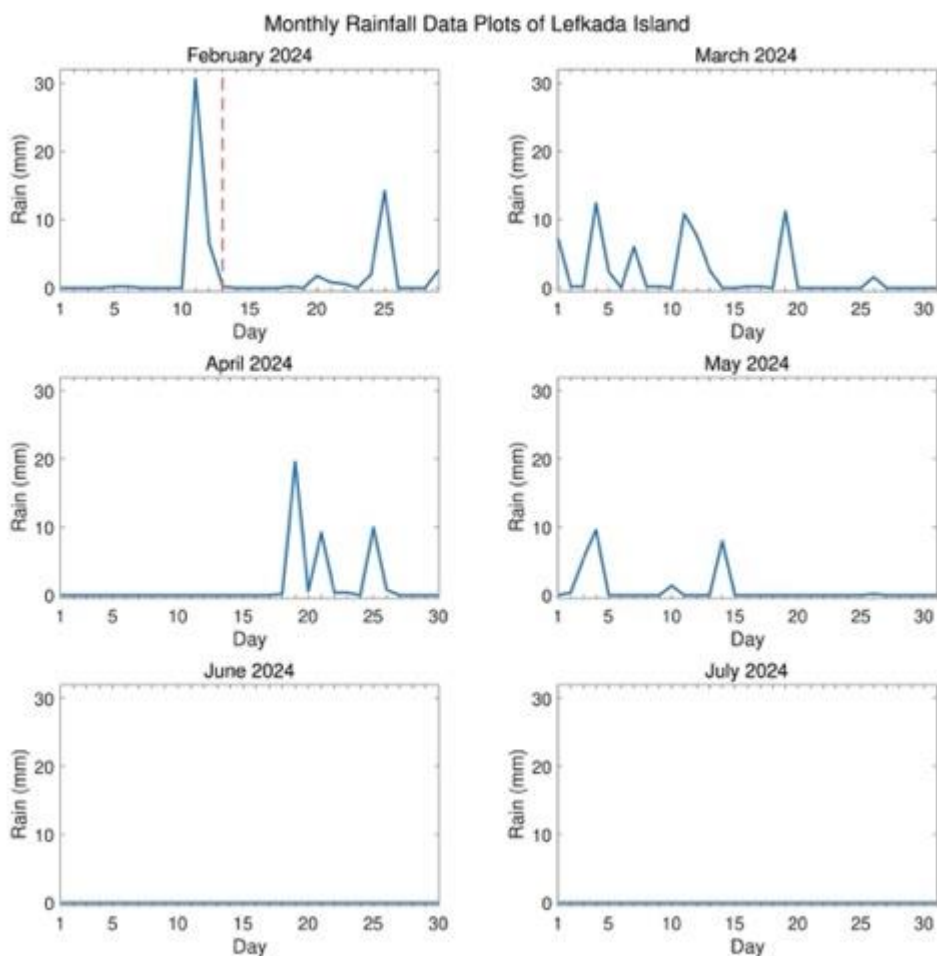


Figure 2.28: Monthly rainfall data plots for Lefkada from February to July 2024 (blue solid lines) compiled from the permanent meteorological station of the National Observatory of Athens (METEO/NOA; <https://meteosearch.meteo.gr>; last accessed 20 August 2024). The vertical red dashed line on the upper left panel of Figure indicates the installation date of the first prototype sensor (13 February 2024).

Complementary to the monthly rainfall data during the target period, the available air temperature (mean, highest and lower values in °C) and the average wind velocity (in km/hr) time-series are also presented. The air temperature and average wind velocity data from February 2024 to July 2024 came from the same data source, namely the permanent meteorological station of Lefkada.

Figure 2.29 presents monthly temperature time-series plots for Lefkada Island from February to July 2024. Each plot displays daily mean, high, and low temperatures, providing insights into the island's temperature variations over these six months. In February 2024, temperatures are relatively cool, with mean temperatures (solid blue line) generally ranging between 10°C and 15°C. The high temperatures (red dashed line) fluctuate between 15°C and 25°C, while the low temperatures (yellow dashed line) are mostly between 5°C and 10°C. March 2024 sees a slight increase in temperatures, with mean temperatures rising closer to 15°C. Highs range between 15°C and 25°C, similarly to February, while lows generally stay above 10°C. The temperature pattern remains relatively stable throughout the month, with small daily fluctuations. April 2024 shows further warming, with mean temperatures ranging between 15°C and 20°C. Highs occasionally reach just above 25°C, and lows stay mostly between 10°C and 15°C. The temperature variability within the month becomes more noticeable, reflecting the transitional nature of spring. In May 2024, the mean temperatures continue to rise, generally staying between 20°C and 25°C. Highs frequently reach above 25°C, with some days nearing 30°C, indicating the approach of Summer. Low temperatures are mostly between 15°C and 20°C, showing a clear warming trend. June 2024 brings more significant warming, with mean temperatures consistently between 25°C and 30°C. High temperatures often exceed 30°C, occasionally nearing 35°C, while lows remain above 20°C. The temperature plots suggest a stable and warm period as summer fully sets in. July 2024 is the warmest month shown, with mean temperatures hovering around 30°C. Highs frequently reach 35°C, and lows rarely drop below 25°C. The temperature data indicates the peak of summer, with very little day-to-day variability, reflecting consistent and sustained warmth. Overall, the data illustrates a clear warming trend from February to July 2024, with temperatures steadily increasing as summer approaches and peaks in July.

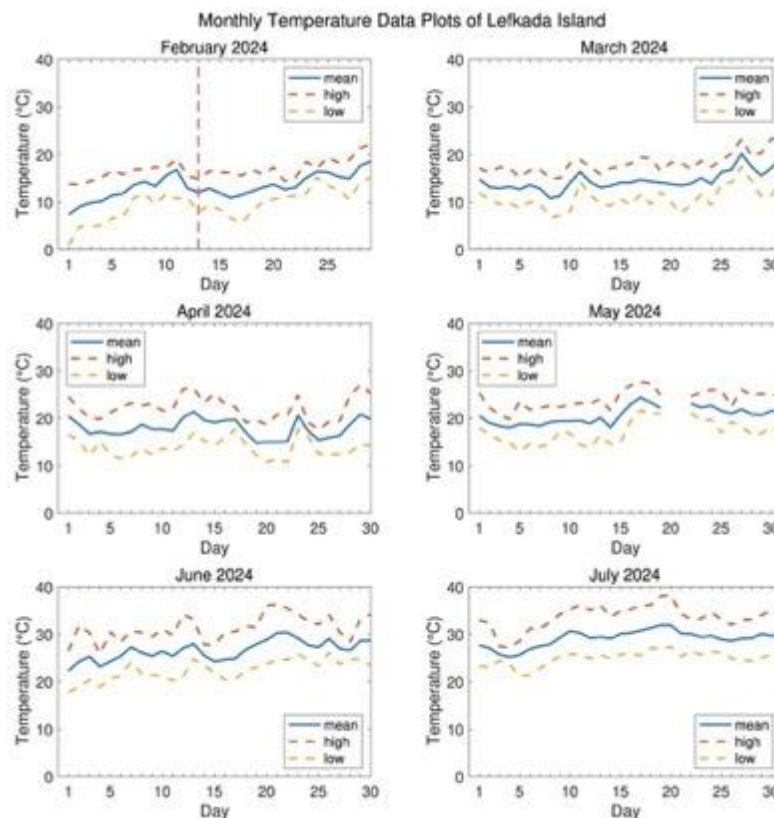


Figure 2.29: Monthly data plots of the lowest (dashed yellow lines), mean (solid blue lines) and highest (dashed brown lines) reported temperatures (°C) for Lefkada from February to July 2024 compiled from the permanent meteorological station of the National Observatory of Athens (METEO/NOA; <https://meteosearch.meteo.gr>; last accessed 20 August 2024). The vertical red dashed line on the upper left panel of figure indicates the installation date of the first prototype sensor (13 February 2024).

Additionally, Figure 2.30 displays the monthly average wind velocity data for Lefkada Island from February to July 2024, with each subplot representing one month. The wind velocity, measured in kilometers per hour (km/hr), is shown as a fluctuating green line across the days of each month. In February 2024, the plot shows relatively low wind velocities at the beginning of the month, generally below 10 km/hr. Around the middle of the month, there's a significant increase of the average wind velocity level, few days before the installation of Brunello Station (13 February; vertical red dashed line). After this point, the wind velocity rises sharply, reaching peaks close to 25 km/hr. March 2024 shows a more variable pattern, with wind velocities ranging from around 5 km/hr to peaks just above 25 km/hr. The wind velocity exhibits several distinct spikes, particularly around the middle and end of the month. In April 2024, the wind velocity remains relatively consistent but still shows some variability, with most days fluctuating between 10 and 20 km/hr. There are occasional peaks approaching 25 km/hr, but these are less pronounced than in other months. May 2024 follows a similar pattern to April, with wind velocities generally staying between 10 and 20 km/hr. There are a few notable spikes early in the month and another towards the middle, reaching up to 25 km/hr. June 2024 exhibits more pronounced variability, with wind speeds frequently rising above 20 km/hr and peaking close to 25 km/hr several times throughout the month. The wind patterns in June suggest a more turbulent period compared to earlier months. Finally, July 2024 shows a slight reduction in variability, with wind velocities mostly ranging between 10 and 20 km/hr. There are fewer significant peaks compared to June, and the wind speed appears more stable, though still fluctuating day-to-day. Summarizing the wind velocity time-series across the target period does not show a consistent seasonal trend, but rather day-to-day variability, with occasional peaks that suggest periods of higher wind activity.

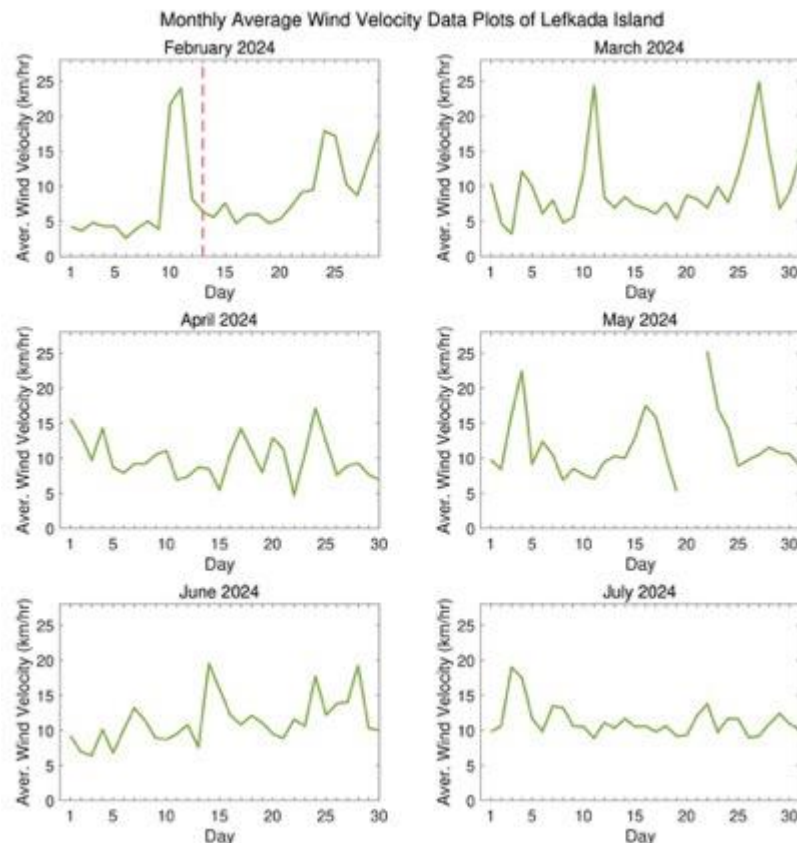


Figure 2.30: Monthly average wind velocity (km/hr) data plots for Lefkada from February to July 2024 (green solid lines) compiled from the permanent meteorological station of the National Observatory of Athens (METEO/NOA; <https://meteosearch.meteo.gr>; last accessed 20 August 2024). The vertical red dashed line on the upper left panel indicates the installation date of the first prototype sensor (13 February 2024).

## 2.5 References

Karakostas, V., Papadimitriou, E., Papazachos, C. 2004. Properties of the 2003 Lefkada, Ionian Islands, Greece, Earthquake Seismic Sequence and Seismicity Triggering. *Bulletin of the Seismological Society of America* 94(5), 1976–1981. <https://doi.org/10.1785/012003254>.

Karakostas, V., Papadimitriou, E., Mesimeri, M., Gkarlaouni, C., Paradisopoulou, P. 2015. The 2014 Kefalonia Doublet (MW6.1 and MW6.0), Central Ionian Islands, Greece: Seismotectonic Implications along the Kefalonia Transform Fault Zone. *Acta Geophysica*, 63(1), 1–16. <https://doi.org/10.2478/s11600-014-0227-4>

Kawabata, K., Sato, T., Takahashi H.A., Tsunomori, F., Hosono, T., Takahashi, M., Kitamura, Y., 2020. Changes in groundwater radon concentrations caused by the 2016 Kumamoto earthquake. *Journal of Hydrology*, 584, 124712.

Kuo, T., Chen W., Lewis, C., Ho, C., Kuochen, H., 2020. Precursory behavior of groundwater radon in Southeastern Taiwan: Effect of tectonic setting in the subduction zone. *Pure and Applied Geophysics*, 177, 2877-2887. <https://doi.org/10.1007/s00024-019-02389-9>

Scholz, C. H. (2019). *The mechanics of earthquakes and faulting*. Cambridge university press. <https://doi.org/10.1017/9781316681473>

## 3 Monitoring the hydrogeological parameters in the Abruzzi region (Italy)

In this section the characteristics of the three sites in which the sensor prototypes were installed in January 2023. They are sites 2 and 3 in the Gran Sasso aquifer and site 8 (Giardino Spring) in Sulmona plain (Figure 3.1).

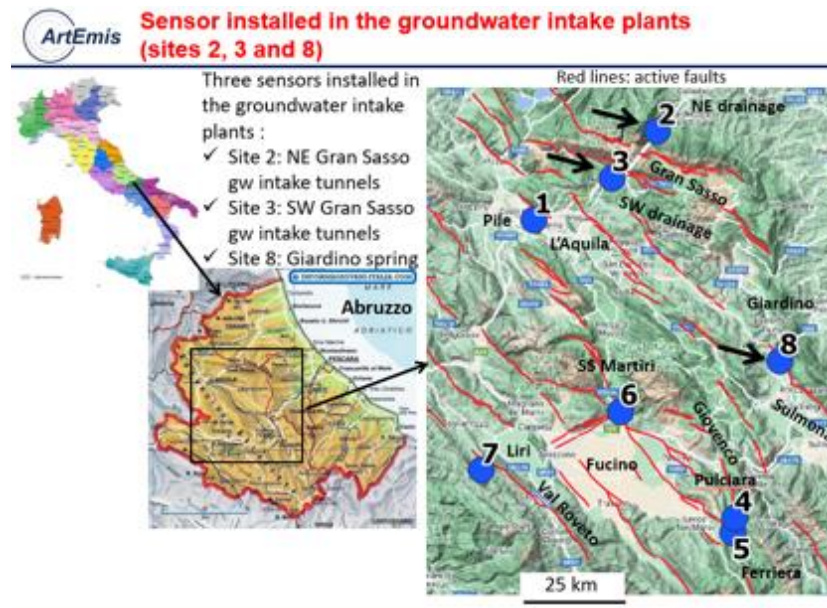


Figure 3.1: Location of the three sites (2, 3 and 8) in which the sensor prototypes were installed in January 2023.

### 3.1 Sensors Installation Sites

#### 3.1.1 Gran Sasso groundwater intake tunnels- sites 2 and 3

In the ArtEmis project, the Gran Sasso aquifer has been selected within the Abruzzo region because significant seismogenic faults and high discharge springs are widespread. Moreover, the Gran Sasso aquifer



The Gran Sasso chain motorway tunnel is made up of two parallel tunnels for both directions, each 10 km long. The two NE (site 2) and SW (site 3) sites drain groundwater collected into the two above-mentioned channels, each 5 km long, and located under the two motorway tunnels (Figures 3.4-3.7). The two channels reach approximately half of the two motorway tunnels, approximately at the surface watershed of the Gran Sasso chain (Figures 3.3). The western and the eastern channels drain groundwater respectively from the western and eastern parts of the Gran Sasso aquifer. Since the Gran Sasso aquifer is fractured and non-porous, the supply of water from the aquifer to the channels is completely discontinuous.

The choice of sites 2 and 3 is based on the following observations:

- (i) groundwater from the two sites flows into the deep core aquifer (the aquifer is protected by 1500-2000 m thick of rock belonging to the undersaturated zone), so it is undisturbed by surface hydrological processes (Figure 3.3);
- (ii) groundwater reaches quickly the sensors because it flows along the channels (it is not groundwater moving slowly in the aquifer, so there is not delay between the “sampling” and the measurement);
- (iii) groundwater flowing in the channels is representative of a quite large portion of the Gran Sasso aquifer (at least 30 km<sup>3</sup>);
- (iv) the Gran Sasso aquifer is crossed by very significant active faults (Assergi and Campo Imperatore faults); e.g., the Campo Imperatore fault is probably causative of the 1349 A.D. Mw 7 earthquake (Galli et al., 2022) (Figures 3.2-3.3);
- (v) the sites show good facilities and logistics.

The local characteristics and installation logistics of the site 2 (NE Gran Sasso groundwater intake tunnels) are reported in the Figures 3.8-3.9. More precisely, in the site 2 the sensor prototype was placed in a plastic tank in which groundwater, spilled from the aqueduct, flows in and out from the tank with a discharge of about 1 L/minute (Figure 3.8).



Figure 3.4: Withdrawal works in the tunnels for draining groundwater (Lunardi and Catalano, 1979).

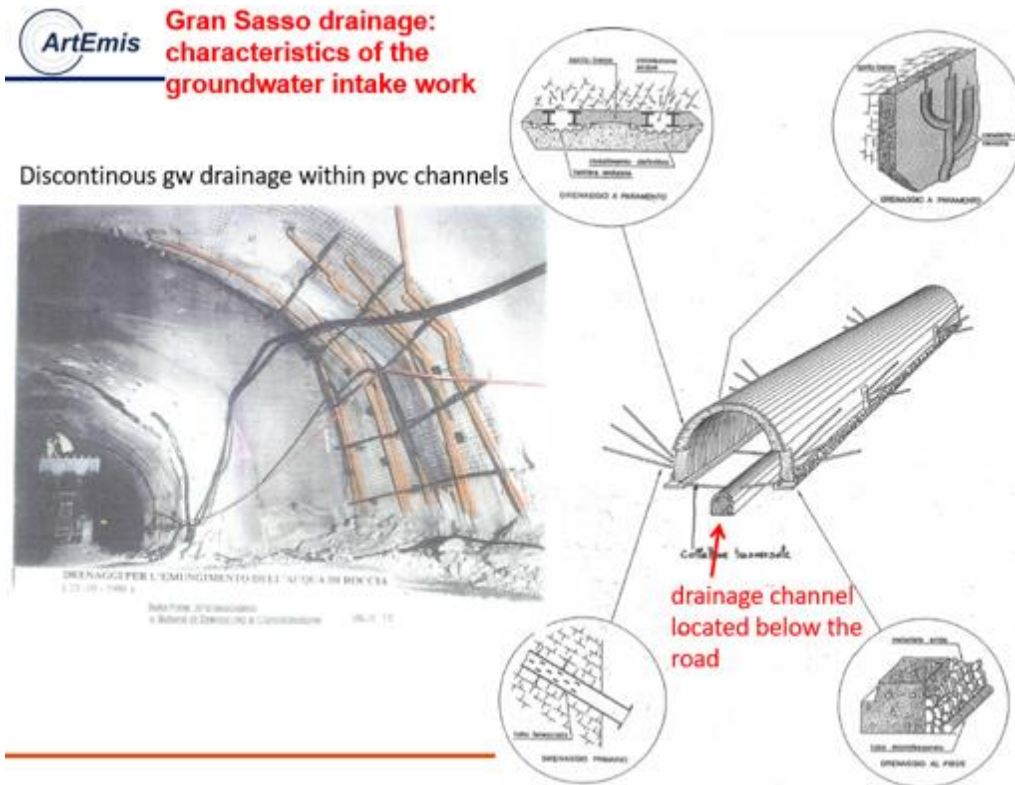


Figure 3.5: Characteristics of the groundwater withdrawal work (hydraulic systems for draining groundwater from the rock mass) (Lunardi and Catalano, 1979).



Figure 3.6: Gran Sasso drainage through channels located below the highway road tunnels.



Figure 3.7: The ending part of the NE Gran Sasso groundwater intake tunnels (picture on the left) and the related hydraulic works (aqueduct – picture on the top right – and control room – picture on the bottom right).



Figure 3.8: Installation logistics of the site 2 (NE Gran Sasso groundwater intake tunnels): tank in which is located the sensor prototype.

**ArtEmis Site 2- sensor installation (Gran Sasso)**



Figure 3.9: Installation logistics of the site 2 (NE Gran Sasso groundwater intake tunnels): transmitter unit and the gateway.

The groundwater withdrawal work of site 3 (SW Gran Sasso groundwater intake tunnels) is reported in the Figures 3.10-3.12, while the local characteristics and installation logistics of the site 3 are reported in the Figures 3.13-3.16. More precisely, in the site 3 the sensor prototype was placed in the accumulation piezometric tank of the water hydraulic work (Figures 3.11, 3.13 and 3.15).

**ArtEmis Site 3- SW Gran Sasso drainage**



Figure 3.10: The site 3 (SW Gran Sasso groundwater intake tunnels): groundwater withdrawal work entrance.

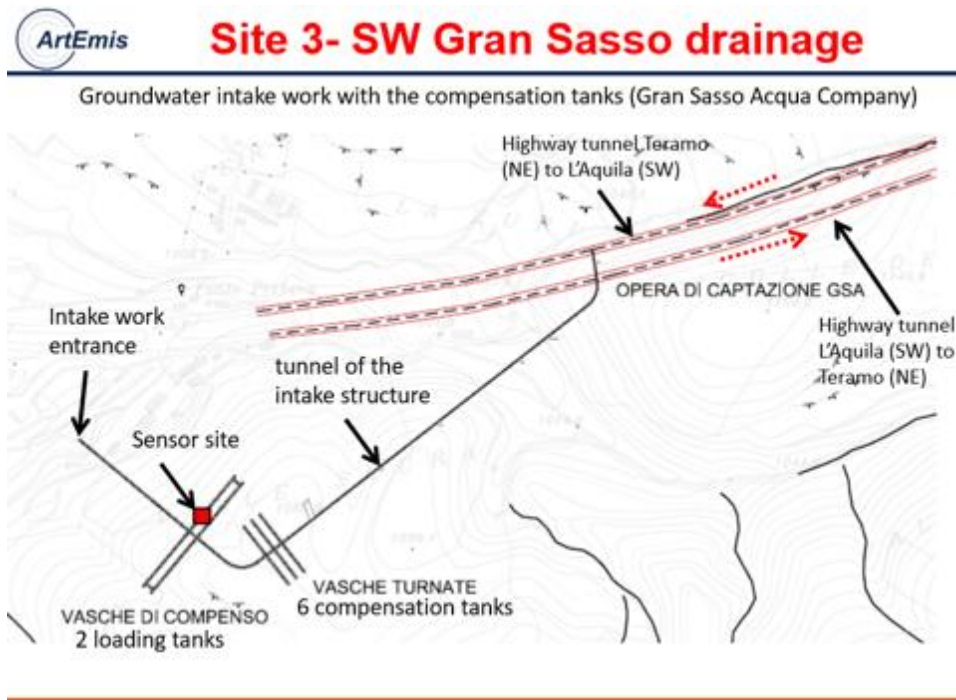


Figure 3.11: The site 3 (SW Gran Sasso groundwater intake tunnels): scheme in plan view of the groundwater withdrawal work in which the location of the sensor prototype is also reported.



Figure 3.12: The site 3 (SW Gran Sasso groundwater intake tunnels): vertical tubes capturing groundwater from the above intake channels. The last are placed just below the highway road Gran Sasso tunnels.

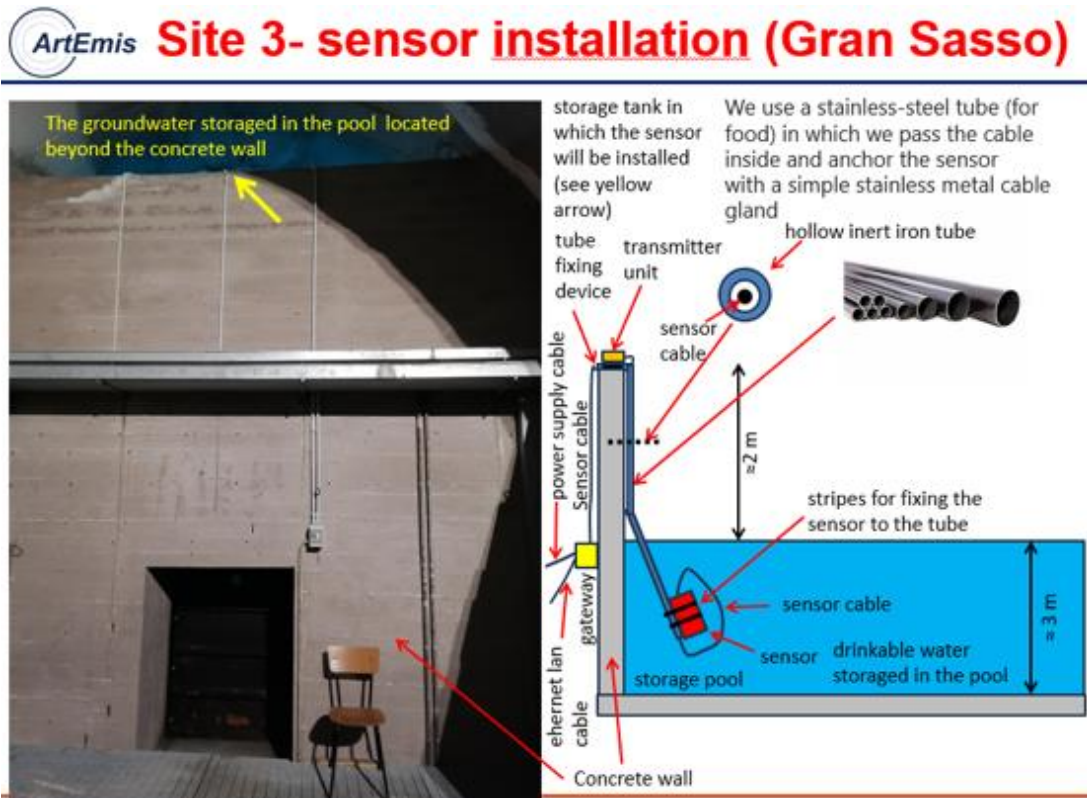


Figure 3.13: Installation logistics of the site 3 (SW Gran Sasso groundwater intake tunnels): site 3 installation scheme.



Figure 3.14: Installation logistics of the site 3 (SW Gran Sasso groundwater intake tunnels): installation activity.



Figure 3.15: Installation logistics of the site 3 (SW Gran Sasso groundwater intake tunnels): the sensor prototype was placed in the accumulation piezometric tank of the water hydraulic work.



Figure 3.16: Installation logistics of the site 3 (SW Gran Sasso groundwater intake tunnels): gateway location.

### 3.1.2 Giardino Spring (Sulmona plain) 每 site 8

In the Sulmona plain, the Giardino Spring (site 8) has been selected as potential monitoring site.

This site is very significant within ArtEmis purposes because the Giardino Spring is placed along the Morrone fault which is considered one of the most relevant seismic gaps of central Italy both for the elapsed time after

the last event (2<sup>nd</sup> century AD?) and the associated maximum expected magnitude (> 6.5) (Ceccaroni et al., 2009; Galli et al., 2015; Gori et al., 2011) (Figure 3.17).

Moreover, hydrogeochemical monitoring of springs and well in the Sulmona plain evidenced an increase above all in the content of As and V in groundwater occurred about four months before the onset of the 2016–2017 central Italy seismic sequence (Barberio et al., 2017).

Finally, in the Giardino Spring, a radon monitoring is going on by Barberio et al. (2018) and with the installation of the ArtEmis sensor we can (i) lengthen the Rn time series and (ii) compare Rn data acquired with ArtEmis sensor with those acquired with the other sensor (Barberio et al., 2018).

In Figures 3.19 and 3.20 are reported the sensor prototype installation and a detail of it, respectively.

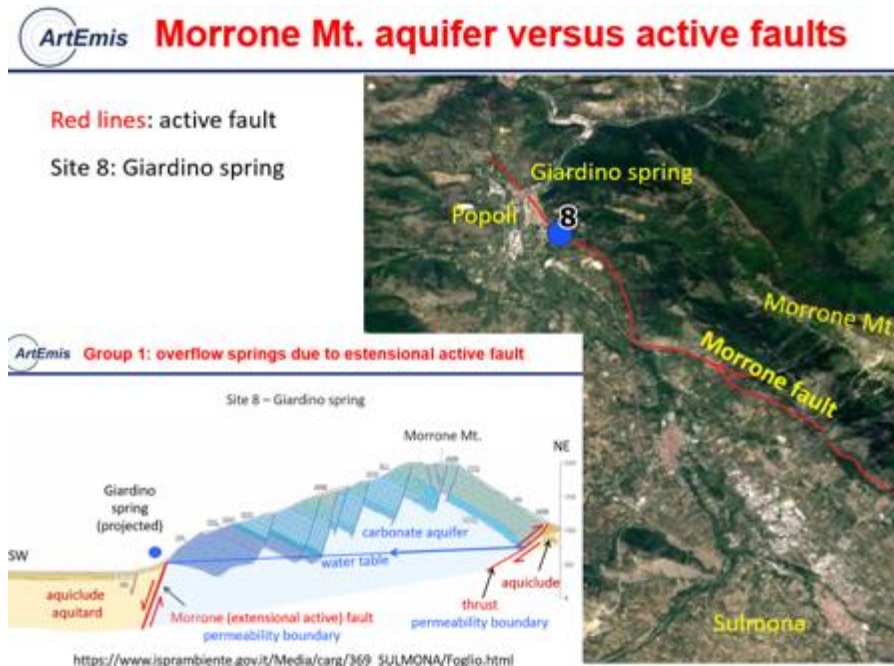


Figure 3.17: Giardino Spring versus the Morrone active fault.



Figure 3.18: Site 8: the Giardino Spring groundwater withdrawal work.

## ArtEmis Site 8- Giardino spring (Sulmona)



Figure 3.19: Giardino Spring (site 8). Sensor prototype installation scheme.

### ArtEmis Roof installed on February 26<sup>th</sup> at Giardino spring (site 8) to protect the transmitter unit



Roof installed on February 26<sup>th</sup> at Giardino spring (site 8) to protect the transmitter unit

Figure 3.20: The Giardino Spring (site 8): Detail of the sensor prototype installation.

### 3.2 Monitoring and operation of the installed sensors

As concerns the three sensor prototypes (site 2, 3 and 8) installed in Abruzzo (Italy), the details regarding (i) the power supply, (ii) the verification of functionality of the three sensor prototypes, (iii) the access to communication and (iv) the test of transmission of data are reported in Table 3.1 and in Figures 3.21-3.25.

#### Site considerations

Important aspects to be considered for the configuration of the systems.

System No.	Site No.	Site name	type	Wifi / mobile	Distance Sensor - transm. transm. – gateway	comments
2	2	NE Gran Sasso tunnel drainage	tank	both	3.5 m 1 m	No pressure sensor and no gyros needed
1	3	SW Gran Sasso tunnel drainage	basin	both	4.5 m 15 m	Deep, might vary
3	8	Giardino spring	„river“	mobile	2.5 m 6 m	Shallow

#### Final tests – 29.01.2024

- Full chain communication test performed: all seems ok.
- Software of „GSI“ Gateway was found to be old and was therefore updated by replacing the SD card with the one from Gateway no. 3
- All four sensor units work well

Table 3.1: Site considerations for the three sensor prototypes in Abruzzo.

#### Test of sensor + Transmitter setup with version V3.1 of Scionix detector - 23.01.2024

Test performed with V3.1 Scionix board + detector No. 1, V1 main board and V1 Transmitter board with firmware installed by BL in December 2023. This setup will be used for the test of the communication with the Gateway. It does not yet include all sensors.

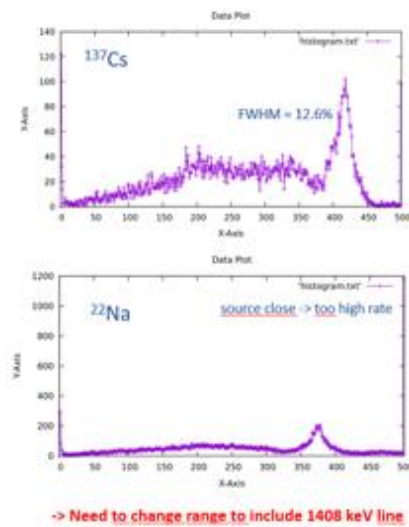


Figure 3.21: Installation of sensor prototypes in Abruzzo: Test of sensor and transmitter setup.

#### Test of voltage drop from gateway to transmitter - 23.01.2024

Test performed with 35 m ethernet cable.

Input 15 V, output 14.77 V at 51 mA -> drop ~ 0.45 V/100 mA

#### Test of newer versions of pcs and firmware - 23.01.2024

Combining V2 of transmitter board (Nov. 06 FW) and V2 of main board (Jan. 22 FW) + V3.1 of Scionix board and using firmware from Nov. 2023 was successful. -> Problems remain mit V3 of transmitter board.

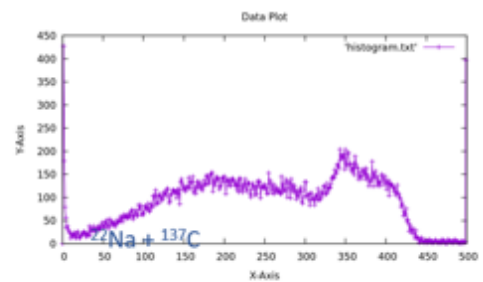


Figure 3.22: Installation of sensor prototypes in Abruzzo: Test of voltage and newer versions of pcs and firmware.

**System 2, site 2 – 31.01.2024**

Composition:

- Csl det. no. 1, Sensor unit S003 V3.1, V2
- Transmitter unit T001 V3 tuned to 5.2V (kept usb cable inside)
- Gateway no. 4 with external 13.5V and 5V supplies connected to two available ac outlets
- D-Link to internet (Italian SIM card), supplied by USB from Transmitter and kept outside to have life signal from blinking.

Mechanics:

- Round plastic tank with H ca. 90 cm, D ca. 75 cm, tightly closed.
- Water inlet on bottom, outlet on top; flow rate adjusted to 0.5l/25s
- 1 cm angled steel rod fixed by screws to the tank. Lower end at the tank center.
- Sensor unit attached by cable binders to the lower end of the steel rod with the ethernet cable running along and exiting through a port stuffed by plastic foil
- 1 m LAN extension cable inserted to obtain the needed length of about 3.5 m.

Site 2:

Located in water station for monitoring water quality. Safe, dry place. Power and mobile net connection available (run by local private water company)  
Installation time 1h, 2 local tech. staff.



Figure 3.23: Sensor prototype installation characteristics of site 2 (NE Gran Sasso groundwater intake tunnels).

**System 1, site 3 – 30.01.2024**

Composition:

- Scionix det. no. 1 (no ext. pressure)
- Sensor unit S004 V3.1, V2
- Transmitter unit T004 V2, tuned to 5.2 V supply
- Gateway „GSI“ with on-board 13.5V and 5V supplies, SD-card no. 3 (outdoor version, originally not planned for indoor use, but no other suitable gateway brought along to the site)
- Ethernet to internet

Mechanics:

- Inverted L-shaped steel plate to be fixed on the rim of a basin holding the transmitter unit (fixed by screwing the housing in threaded holes) and the upper end of a steel tube assembly holding the detector and leading the ethernet cable from Sensor to Transmitter
- Lower end of the upper steel tube is angled by 13° to keep the sensor away from the rim wall.
- Steel tube with 1 m and/or 50 cm long pieces connected by clamps
- Sensor unit attached by cable binders to the lower end of the piping assembly with the ethernet cable running inside

Site 3:

Several 100 m inside a tunnel; water basin behind a 5 m high thick wall with a water level of currently 3.6 m; basin width about 6 m; sensor depth ≈2 m  
Power and internet connection available (multi-sensor system run by local private water company).  
Installation time 3h, 5 local tech. staff



Figure 3.24: Sensor prototype installation characteristics of site 3 (SW Gran Sasso groundwater intake tunnels).

**System 3, site 8 – 31.01.2024**

Composition:

- Scionix det. no. 2, Sensor unit S002 V3.1, V2
- Transmitter unit T002 V2 tuned to 5.2V
- Gateway no. 5 with external 13.5V and 5V supplies connected to two available ac outlets
- D-Link to internet (Italian SIM card), supplied by USB from Gateway and kept inside watertight box.

Mechanics:

- Water inlet pipe close to sensor to have truly flowing water.
- 1.5 m angled steel tube (D(i) = 2.2 cm) fixed by clamps to a 1.5 mm thick steel plate bolted to the concrete wall
- Sensor unit attached by cable binders to the lower end of the steel tube with the ethernet cable running inside and exiting to the Transmitter unit screwed onto the steel plate.
- Water height ca. 50 cm, sensor placed at about 25 cm from bottom and ca. 50 cm from wall.
- Gateway, power supplies and D-link housed in a watertight box below a concrete bridge for best protection.

Site 8:

Flowing water from a spring in a concrete bed  
 Power and mobile net connection available (run by local private water company)  
 Installation time 1.5h, 2 local tech. staff.



Figure 3.25: Sensor prototype installation characteristics of site 8 (Giardino Spring).

In the Figures 3.26-3.29, the mean values of the sensor parameters and the obtained Rn spectrum are reported for the sites 2 and 3.



**Sensor Reports (Mean values)**

**Site 2: NE Gran Sasso groundwater intake tunnels (system 2)**

<b>Gamma count rate</b>	1 counts per second in all channels(500 channels)
<b>Pressure inside the casing</b>	916.2 hPa
<b>Temperature</b>	17.9 C
<b>Humidity</b>	60.4%
<b>Sensor level above sea</b>	840.08m
<b>Microphone value</b>	868(noise level)
<b>Peak position shifting</b>	No
<b>Histogram Scale</b>	5

Figure 3.26: Report of the sensor prototype installed in site 2.



**NE Gran Sasso tunnel drainage Rn spectrum (site 2)**

**Radon Spectrum**

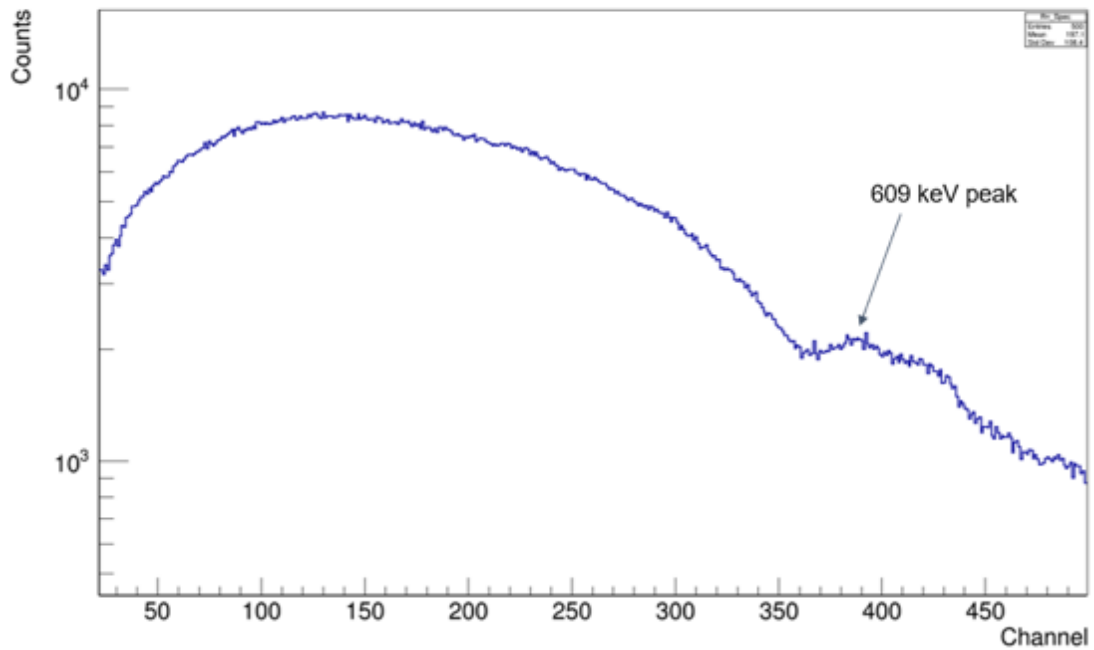


Figure 3.27: Rn spectrum obtained by sensor prototype installed in site 2.



**Sensor Reports (Mean values)**

**Site 3: SW Gran Sasso groundwater intake tunnels (system 1)**

<b>Gamma count rate</b>	3 counts per second in all channels(500 channels)
<b>Pressure inside the casing</b>	907.62 hPa
<b>Temperature</b>	9.92 C
<b>Humidity</b>	55.04%
<b>Sensor level above sea</b>	919 m
<b>Microphone value</b>	932 (noise level)
<b>Peak position shifting</b>	No
<b>Histogram Scale</b>	5

Figure 3.28: Report of the sensor prototype installed in site 3.



**SW Gran Sasso groundwater intake tunnels (site 3) Rn spectrum**

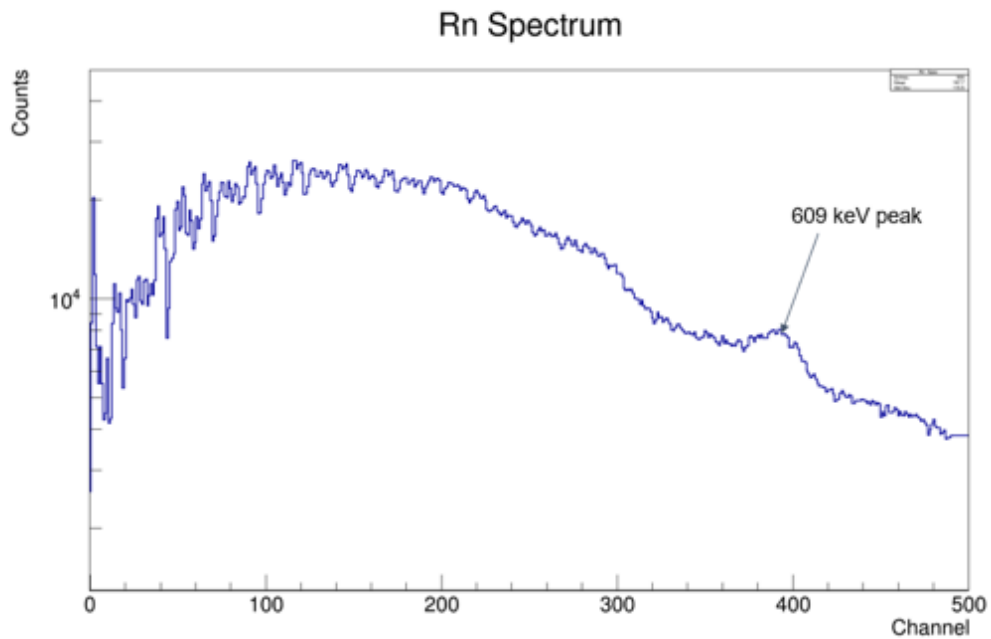


Figure 3.29: Rn spectrum obtained by sensor prototype installed in site 3.

As an example, the Radon pre-processed data is reported in Figure 3.30 (Törngren, 2024).

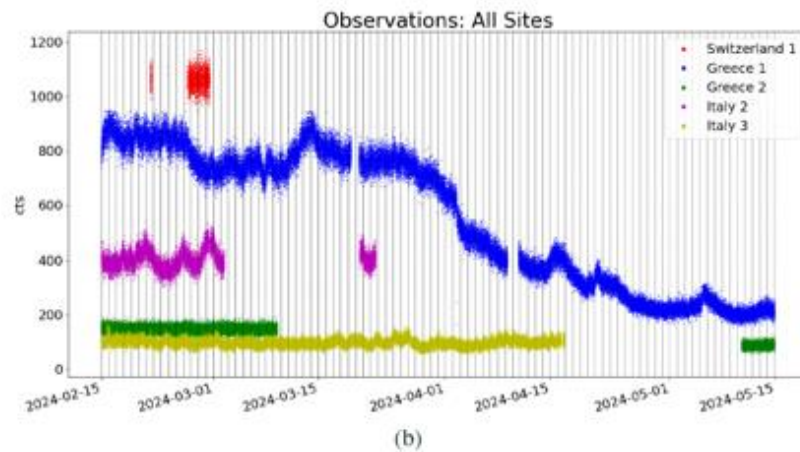
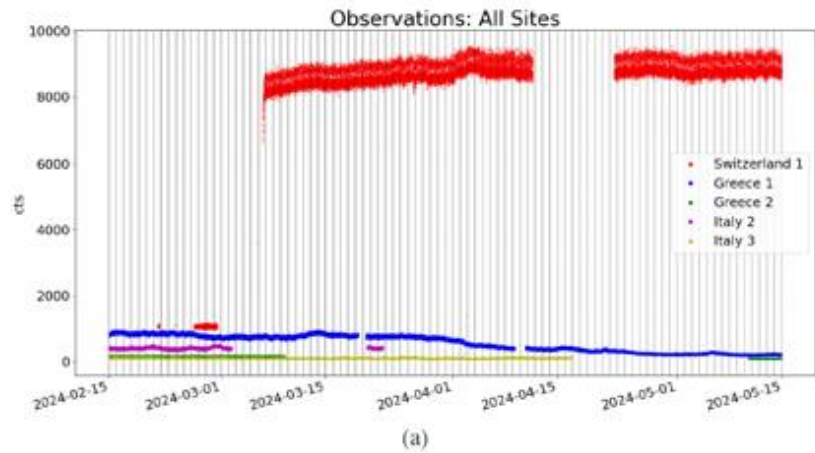


Figure 3.30: Pre-processed data: (a) all data and (b) limited count range for a clearer view of sites with lower count rate (time: 15 Feb-15 May 2024) (Italy 2: site 2; Italy 3: site 3) (Törngren, 2024).

### 3.3 Monitoring of the hydrogeological parameters during the target period

The Radon data measured in groundwater by the ArtEmis sensor prototypes must be compared with seismicity, but also with hydrogeological and meteo-climatic data to evaluate how the hydrogeological setting can influence the Radon value. In this way, by comparing Radon data with meteo-climatic ones, the noise background of Radon in groundwater can be estimated for the Abruzzo region.

For sites 2, 3 and 8 many hydrogeological and meteorological-climatic data are available (Tables 3.2-3.4). The meteo-climatic data (above all air temperature and rainfall) were provided by the Hydrographic and Mareographic Service of the Abruzzo region. The groundwater discharge and hydrochemical data were provided by the Abruzzo Water companies, and more precisely, by Ruzzo Reti, Gran Sasso Acqua and ACA for sites 2, 3 and 8, respectively (Figures 3.31-3.47). In the continuation of the project, the above-mentioned institutions will continue to provide us with the time series of the above-mentioned data. We take this opportunity to thank the above-mentioned institutions for providing us with these environmental dates. For site 2, a very complete set of hydrochemical and hydrogeological data acquired at high frequency, such as discharge, groundwater temperature, electrical Conductivity, pH, redox potential, Total Organic Carbon and turbidity, are available (Figures 3.31-3.36). This availability could be very useful to analyse the Radon background noise in the Gran Sasso groundwater.

Meteo-climatic data	Gw discharge	Hydrochemical data
Air temperature rainfall Air humidity Wind velocity and direction meteo station: Campo Imperatore (acquisition frequency: 15 minutes)	Gw discharge (acquisition frequency: hourly)	Gw T, EC, pH, ORP, TOC, Turbidity (acquisition frequency: 4 minutes)

Table 3.2: Site 2: available meteo and hydrogeological data (time: Jan 1<sup>st</sup>-June 30<sup>th</sup> 2024). Gw: groundwater, T: temperature (°C), ORP: redox potential (mV), TOC: Total Organic Carbon (ppm).

Meteo-climatic data	Gw discharge
Air temperature and rainfall meteo station: Assergi (acquisition frequency: 15 minutes)	Gw discharge water height (acquisition frequency: daily)

Table 3.3: Site 3: available meteo and hydrogeological data (time: Jan 1<sup>st</sup>-June 30<sup>th</sup> 2024).

Meteo-climatic data	Gw discharge
Air temperature and rainfall meteo station: Sulmona (acquisition frequency: 15 minutes)	Gw discharge (acquisition frequency: 1-2 minutes)

Table 3.4: Site 8: available meteo and hydrogeological data (time: Jan 1<sup>st</sup>-June 30<sup>th</sup> 2024).

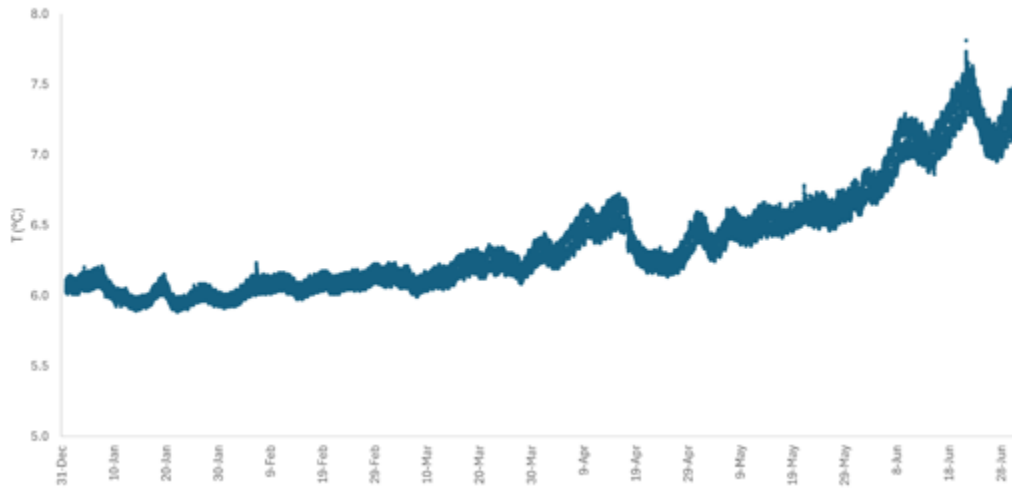


Figure 3.31: Site 2 groundwater temperature versus time (time: January 1<sup>st</sup> – June 30<sup>th</sup> 2024). Acquisition frequency: 4 minutes.

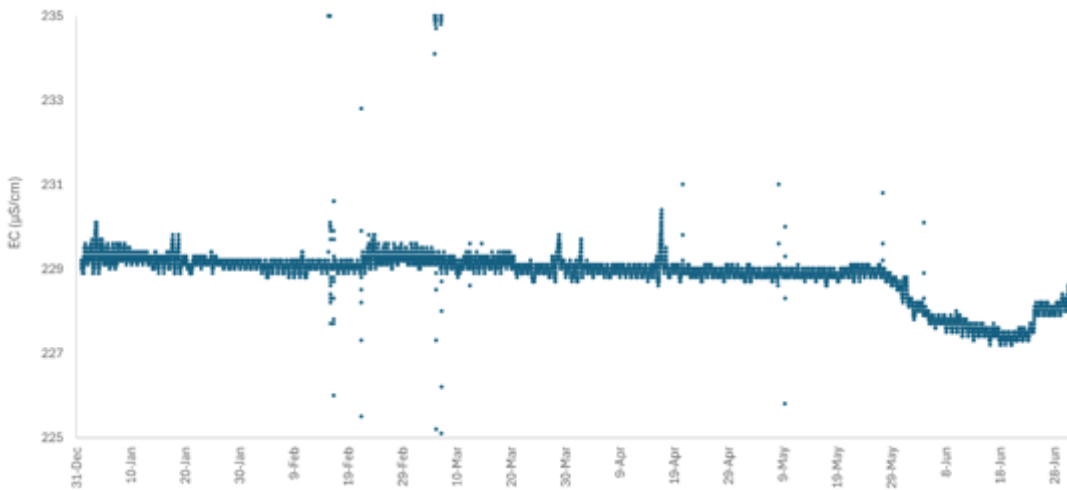


Figure 3.32: Site 2 groundwater Electrical Conductivity (EC) versus time (time: January 1<sup>st</sup> – June 30<sup>th</sup> 2024). Acquisition frequency: 4 minutes.

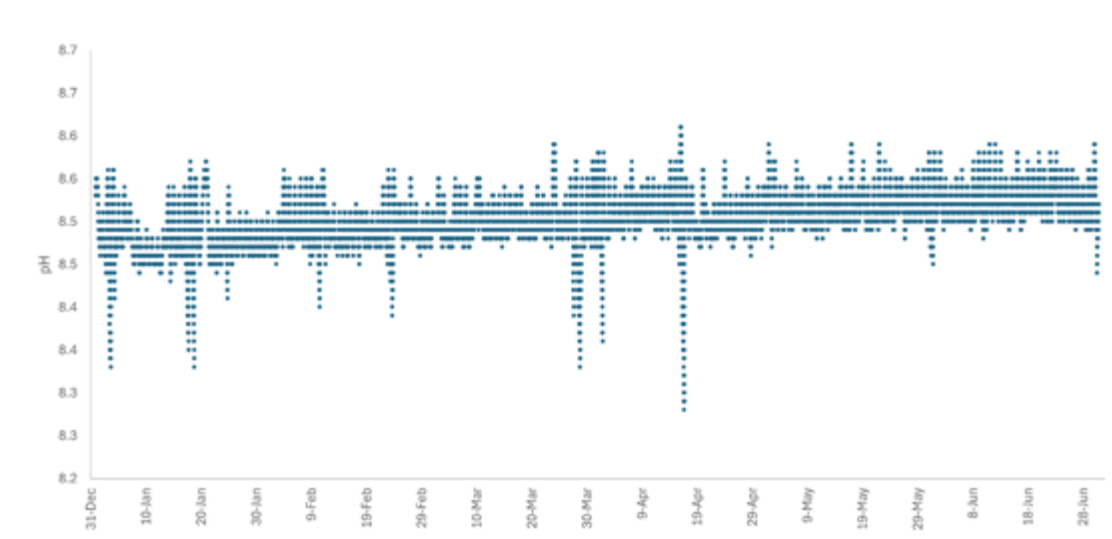


Figure 3.33: Site 2 groundwater pH versus time (time: January 1<sup>st</sup> – June 30<sup>th</sup> 2024). Acquisition frequency: 4 minutes.

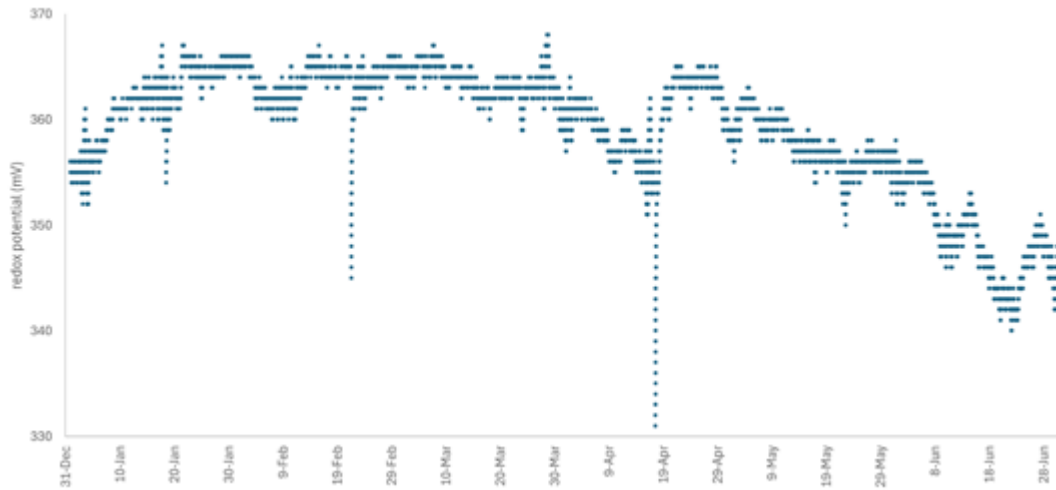


Figure 3.34: Site 2 groundwater redox potential versus time (time: January 1<sup>st</sup> – June 30<sup>th</sup> 2024). Acquisition frequency: 4 minutes.

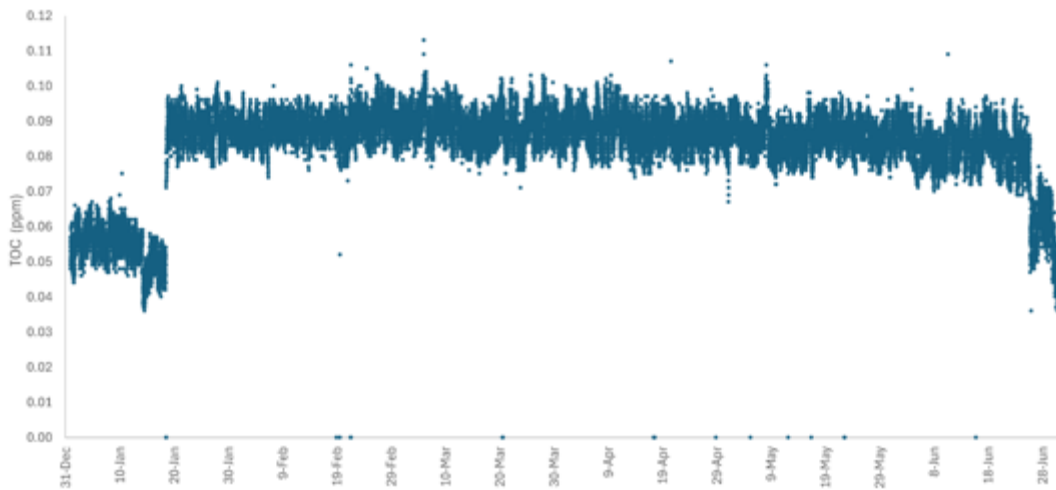


Figure 3.35: Site 2 groundwater Total Organic Carbon (TOC) versus time (time: January 1<sup>st</sup> – June 30<sup>th</sup> 2024). Acquisition frequency: 4 minutes.

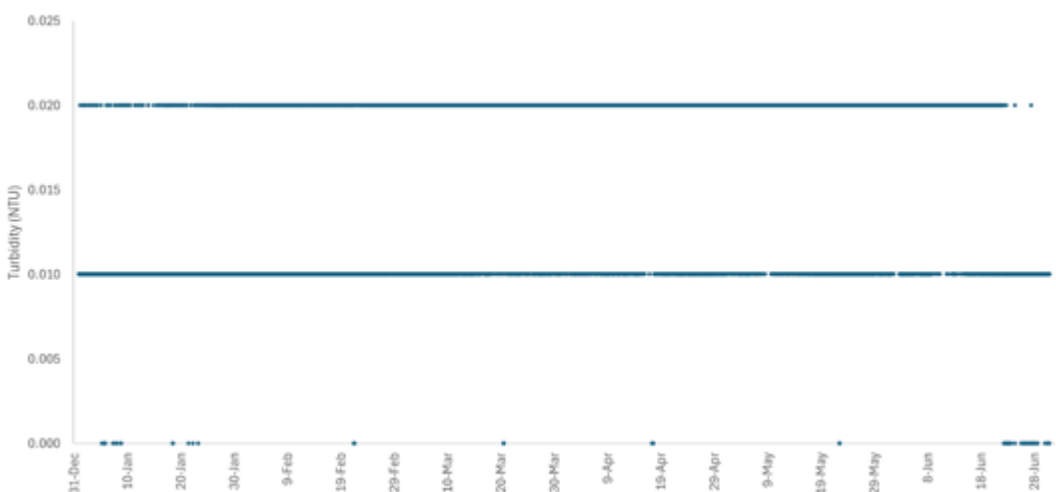


Figure 3.36: Site 2 groundwater turbidity versus time (time: January 1<sup>st</sup> – June 30<sup>th</sup> 2024). Acquisition frequency: 4 minutes.

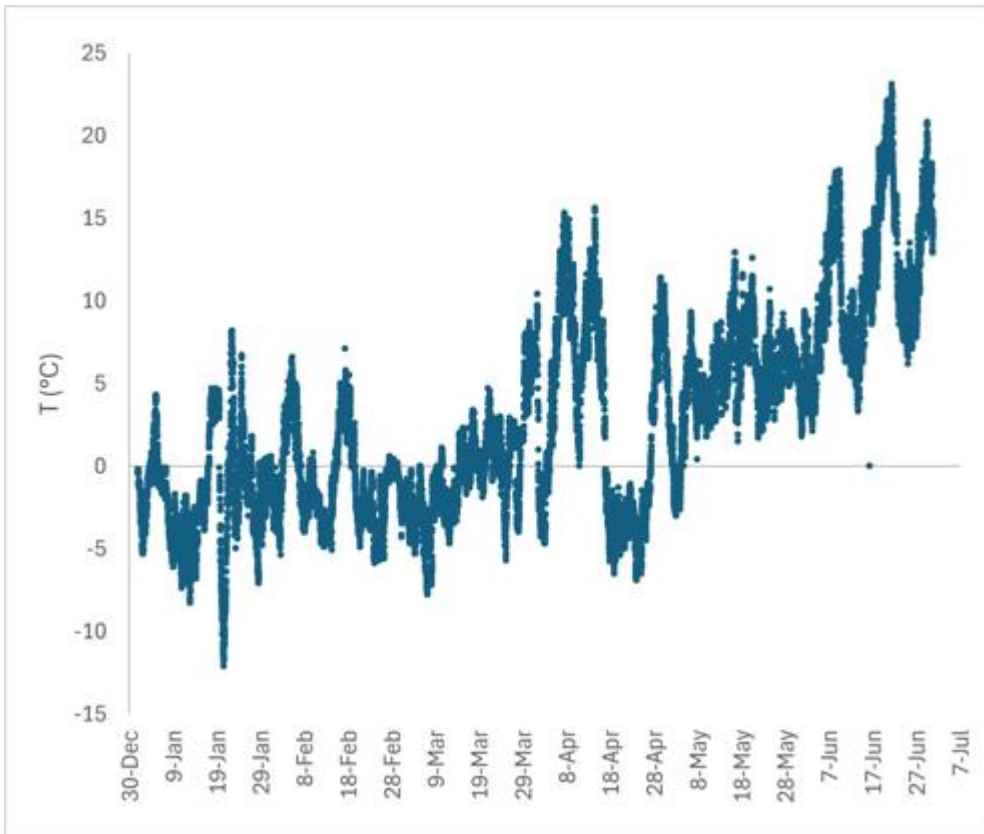


Figure 3.37: Site 2 air temperature (meteo station: Campo Imperatore) (time: January 1<sup>st</sup> – June 30<sup>th</sup> 2024). Acquisition frequency: 15 minutes.

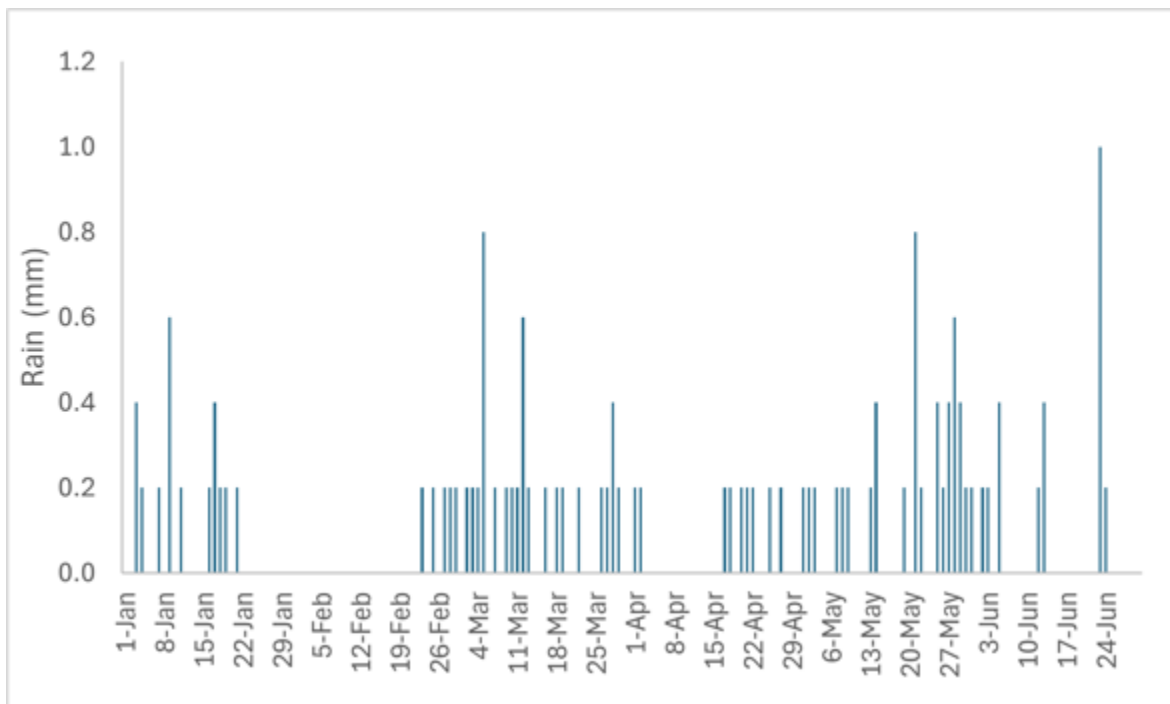


Figure 3.38: Site 2 rainfall (meteo station: Campo Imperatore) (time: January 1<sup>st</sup> – June 30<sup>th</sup> 2024). Acquisition frequency: 15 minutes.

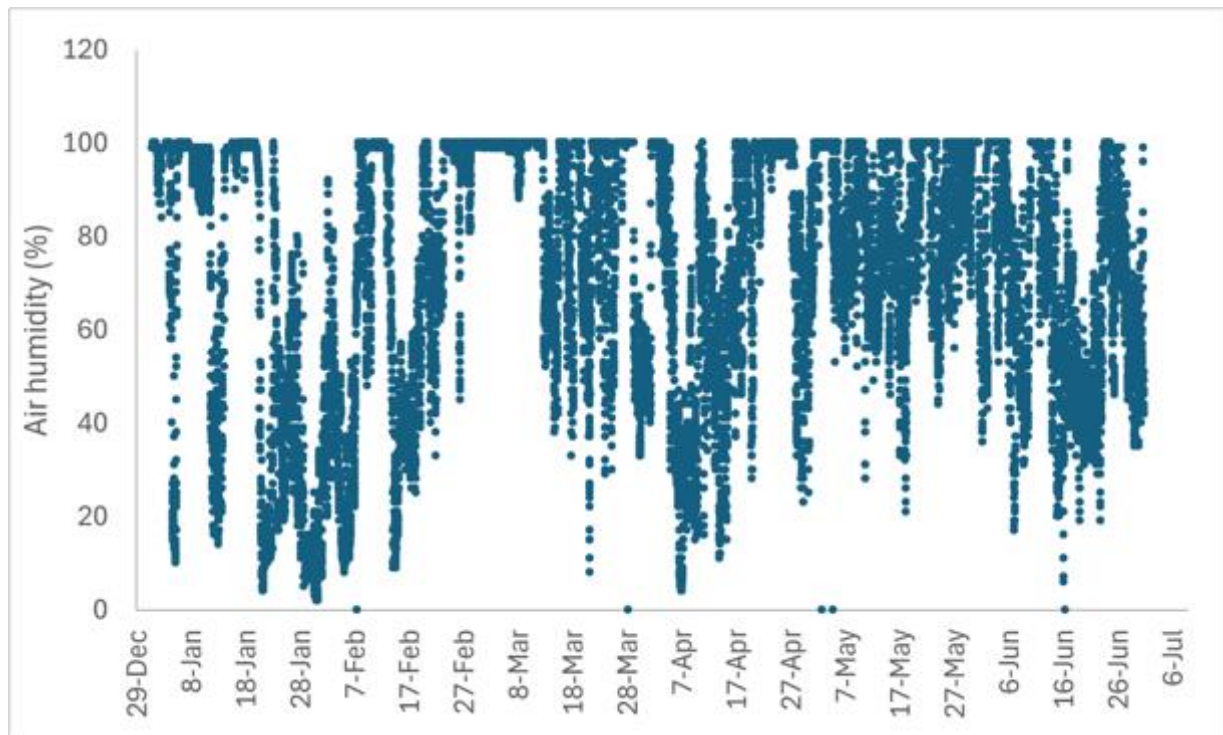


Figure 3.39: Site 2 air humidity (%) (meteo station: Campo Imperatore) (time: January 1<sup>st</sup> – June 30<sup>th</sup> 2024). Acquisition frequency: 15 minutes.

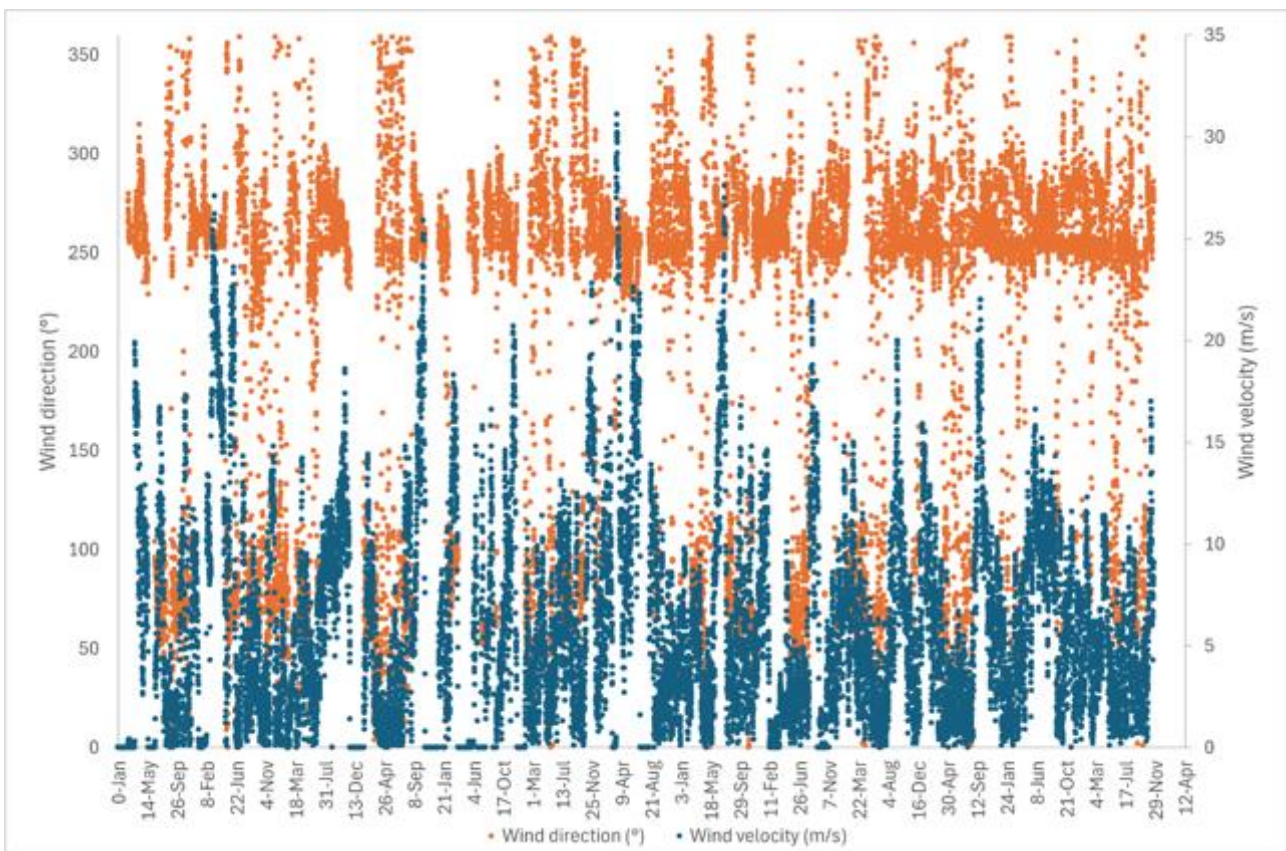


Figure 3.40: Site 2 wind direction and velocity (meteo station: Campo Imperatore) (time: January 1<sup>st</sup> – June 30<sup>th</sup> 2024). Acquisition frequency: 15 minutes.

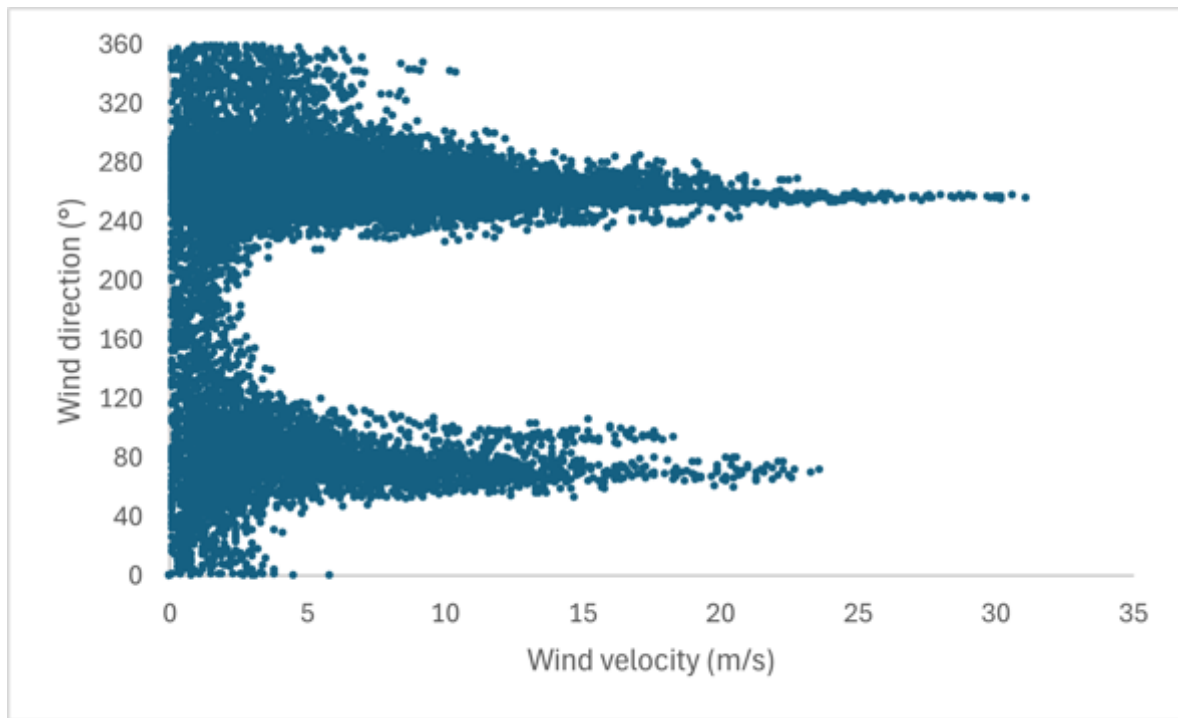


Figure 3.41: Site 2 wind Direction versus wind velocity (meteo station: Campo Imperatore) (time: January 1<sup>st</sup> – June 30<sup>th</sup> 2024). Acquisition frequency: 15 minutes.

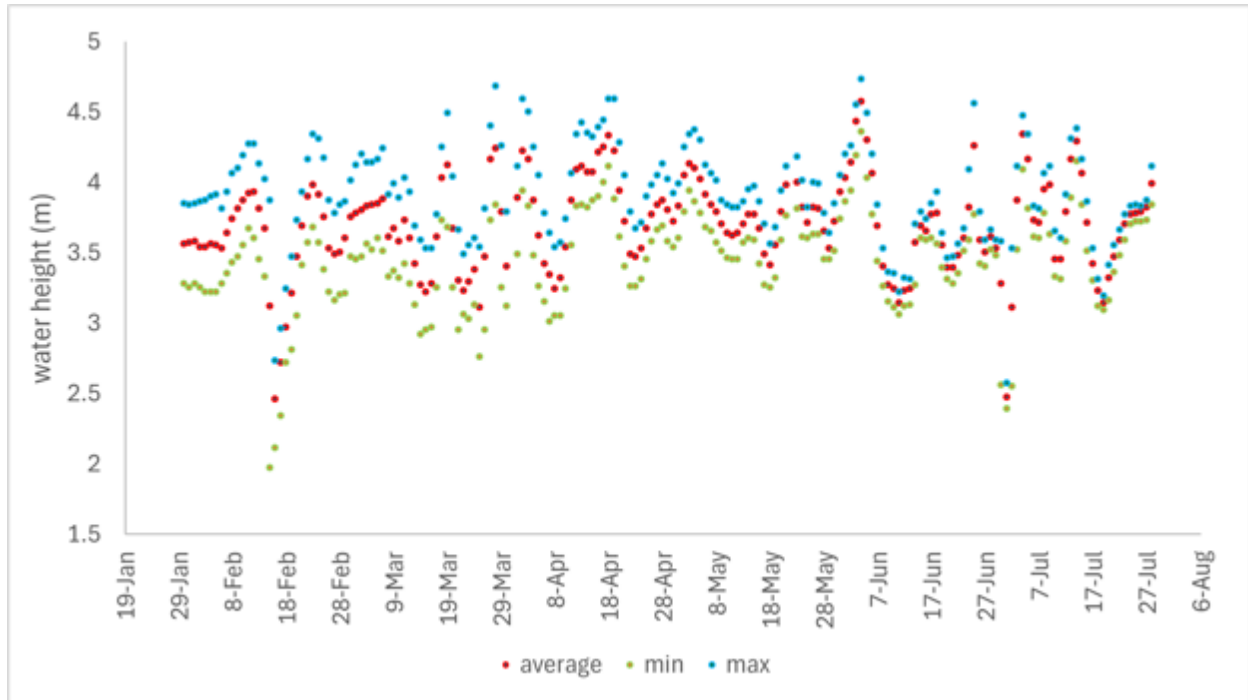


Figure 3.42: Site 3: water height in the groundwater storage pool in which the sensor prototype is placed (see Figs. 3.15 and 3.24) (time: January 30<sup>th</sup> – July 28<sup>th</sup> 2024). Acquisition frequency: daily.

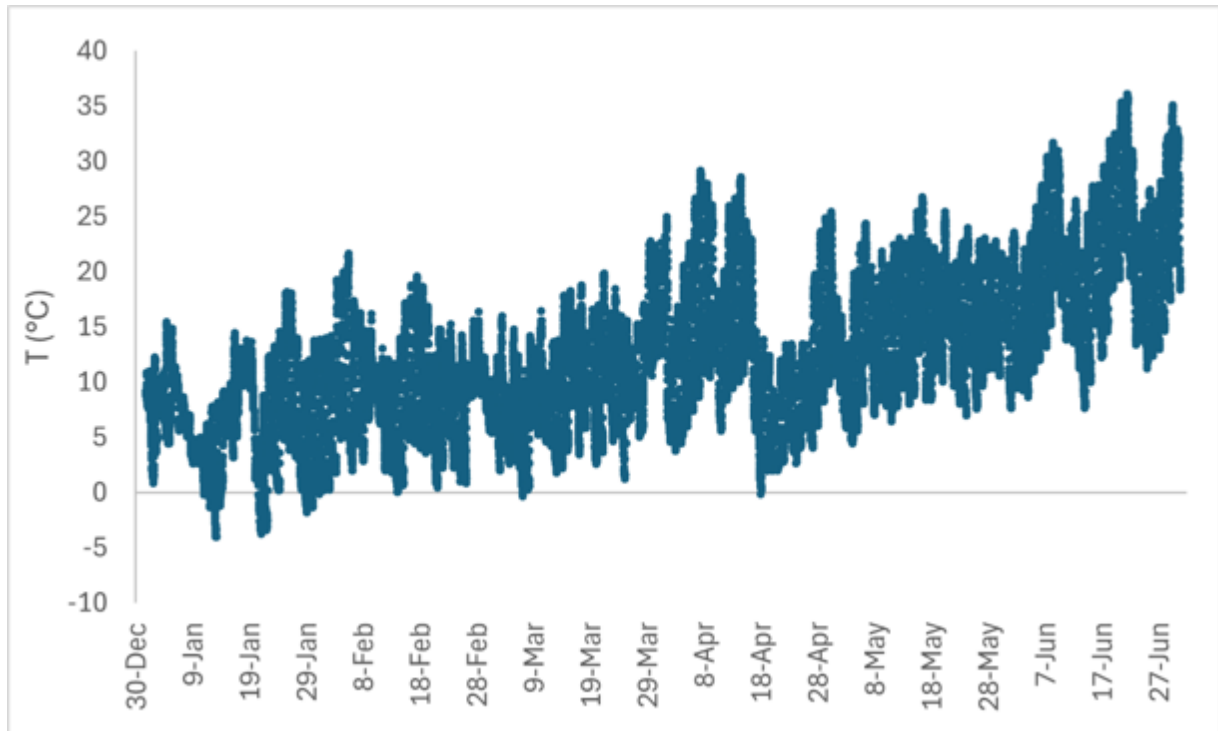


Figure 3.43: Site 3 air temperature (meteo station: Assergi) (time: January 1<sup>st</sup> – June 30<sup>th</sup> 2024). Acquisition frequency: 15 minutes.

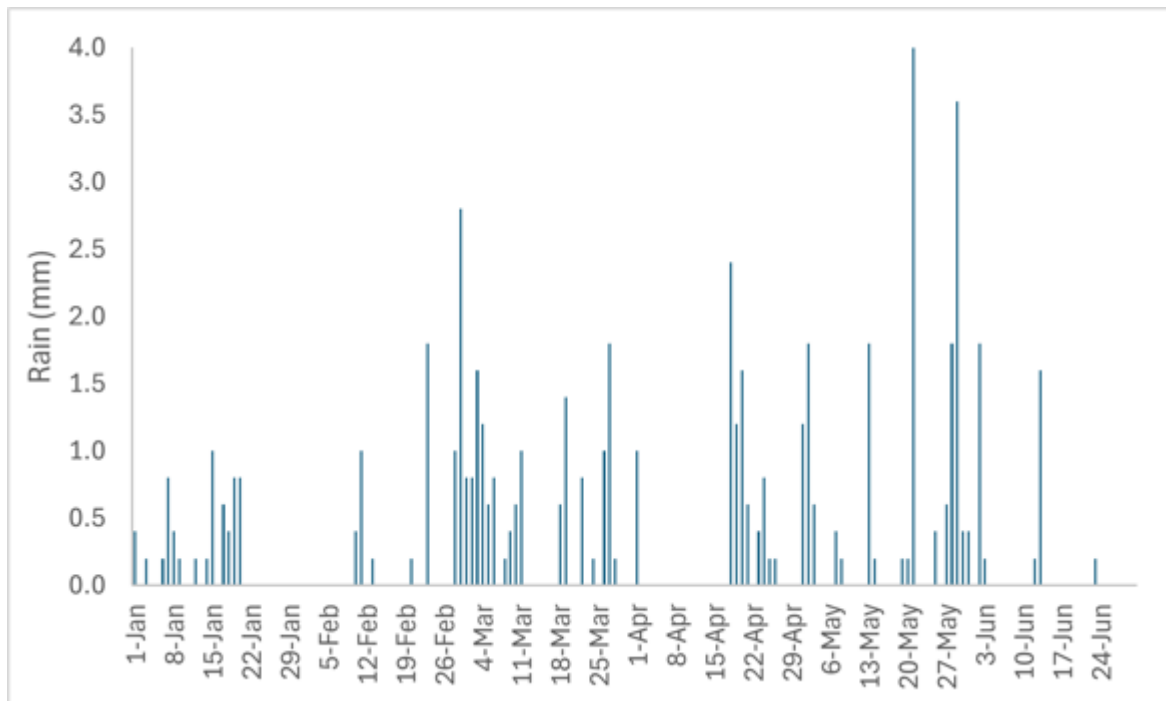


Figure 3.44: Site 3 rainfall (meteo station: Assergi) (time: January 1<sup>st</sup> – June 30<sup>th</sup> 2024). Acquisition frequency: 15 minutes.

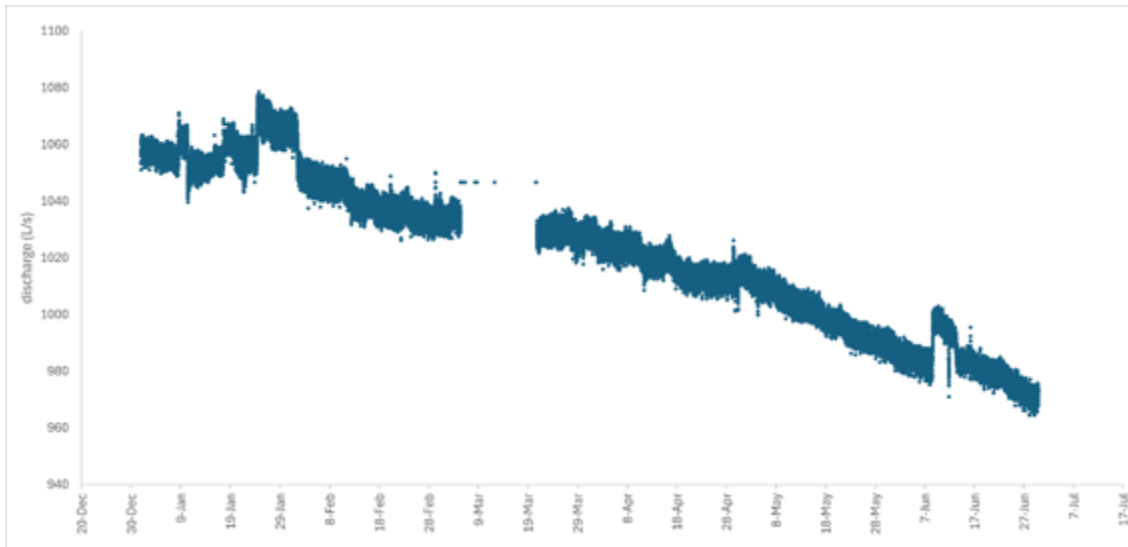


Figure 3.45: Site 8: groundwater discharge of Giardino Spring (time: January 1<sup>st</sup> – June 30<sup>th</sup> 2024). Acquisition frequency: 1-2 minutes.

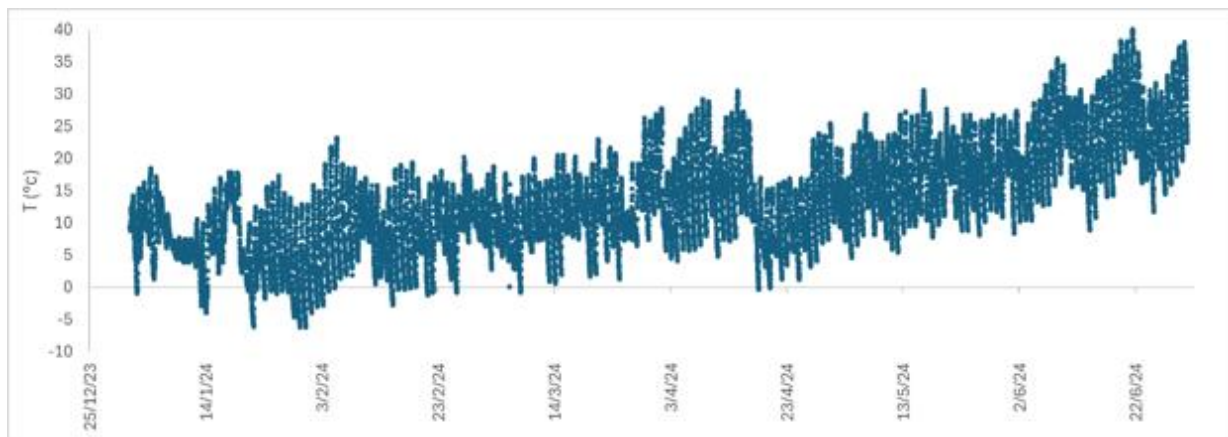


Figure 3.46: Site 8 air temperature (meteo station: Sulmona) (time: January 1<sup>st</sup> – June 30<sup>th</sup> 2024). Acquisition frequency: 15 minutes.

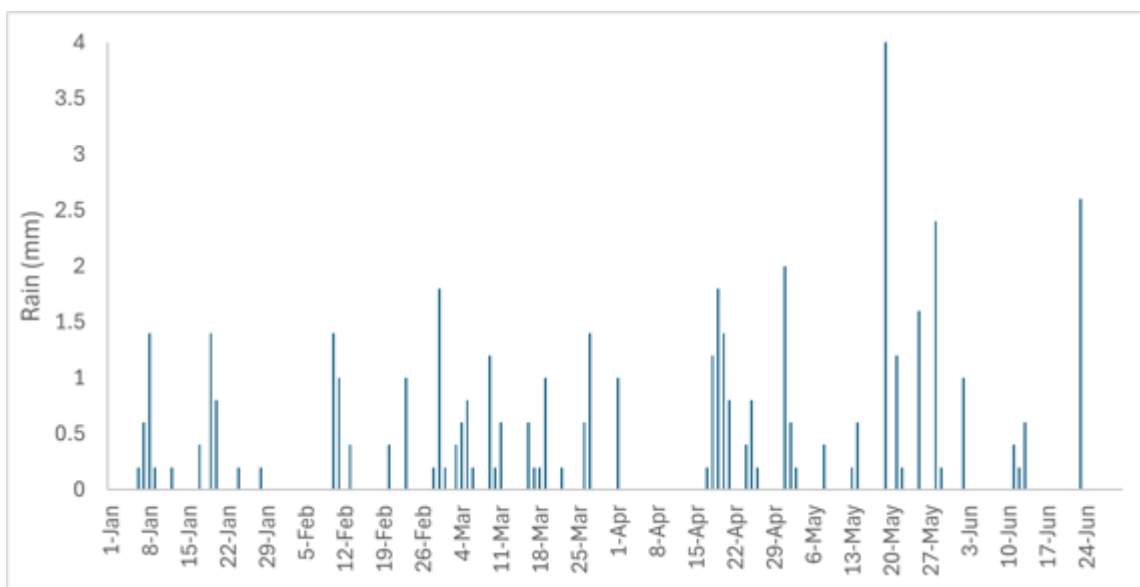


Figure 3.47: Site 8 rainfall (meteo station: Sulmona) (time: January 1<sup>st</sup> – June 30<sup>th</sup> 2024). Acquisition frequency: 15 minutes.

### 3.4 References

- Barberio, M.D., Barbieri, M., Billi, A., Doglioni, C., Petitta, M., 2017. Hydrogeochemical changes before and during the 2016 Amatrice-Norcia seismic sequence (central Italy). *Scientific Reports* 7, 11735. <https://doi.org/10.1038/s41598-017-11990-8>.
- Barberio, M. D., Gori, F., Barbieri, M., Billi, A., Devoti, R., Doglioni, C., Petitta, M., Riguzzi, F., Rusi, S., 2018. Diurnal and semidiurnal cyclicity of radon ( $^{222}\text{Rn}$ ) in groundwater, Giardino Spring, Central Apennines, Italy. *Water*, 10(9). [1276. 10.3390/w10091276](https://doi.org/10.3390/w10091276).
- Ceccaroni, E., Ameri, G., Capera, A.A.G., Galadini, F., 2009. The 2nd century AD earthquake in central Italy: archaeoseismological data and seismotectonic implications. *Natural hazards* 50(2), 335-359.
- De Luca, G., Di Carlo, G., Tallini, M., 2018. A record of changes in the Gran Sasso groundwater before, during and after the 2016 Amatrice earthquake, central Italy. *Scientific Reports* 8 (1), 1–16. <https://doi.org/10.1038/s41598-018-34444-1>.
- Galli, P., Giaccio, B., Peronace, E., Messina, P., 2015. Holocene Paleearthquakes and Early–Late Pleistocene Slip Rate on the Sulmona Fault (Central Apennines, Italy). *Bulletin of the Seismological Society of America*, 105(1), 1-13.
- Gori, S., Giaccio, B., Galadini, F., Falcucci, E., Messina, P., Sposato, A., Dramis, F., 2011. Active normal faulting along the Mt. Morrone south-western slopes (central Apennines, Italy). *International journal of earth sciences* 100(1), 157-171.
- Isaya D., De Luca G., Tallini M. (2024) - Detection capability of earthquakes by a hydraulic pressure device in the Gran Sasso aquifer (central Italy). Congress GNGTS2024, Ferrara, February 13-16, 2024, [https://gngts.ogs.it/wp-content/uploads/2024/01/11\\_Abstract\\_GNGTS2024.pdf](https://gngts.ogs.it/wp-content/uploads/2024/01/11_Abstract_GNGTS2024.pdf), 138-143.
- Lunardi, P., Catalano, P., 1979. Gran Sasso. Il traforo autostradale [Gran Sasso. The highway tunnels]. Gangemi Editore.
- Törngren, P. K., 2024. Inferring Changes in Groundwater Radionuclide Concentration. A Step towards Earthquake Forecasting using Measurements of Groundwater Radioactivity. Degree Project in the Field of Technology and the Main Field of Study Engineering Physics, Second cycle, Supervisors: Torbjörn Bäck, Gregory Nuel; Examiner: Ayşe Ataç Nyberg, School of Engineering Sciences. KTH, Royal Institute of Technology, Stockholm.

## 4 Monitoring the hydrogeological parameters in the Swiss Alps and Bedretto Lab

### 4.1 Sensors Installation Sites

The geographical and geological description of the installation of the ArtEmis sensor in Bedretto (TI) in the Swiss Alps, has already been extensively described in previous deliverables (see also e.g., Keller and Schneider, 1982; Ma et al., 2022; Rast et al., 2022). The Bedretto tunnel (Figure 4.1) is located in an area with comparably low seismic hazard in Switzerland (Wiemer et al., 2016). Only a few earthquakes with magnitudes larger than 2.5 occurred since 1975 in within 30 km from the tunnel entrance, with the largest having a  $M_L$  of 4.0 (in Oberwald, VS, 01.07.2021; SED 2023). FEAR (FEAR 2024; Fault activation and earthquake rupture) aims to conduct a suite of ambitious experiments within the Bedretto lab. The idea is to better understand how earthquakes start and stop by using hydraulic stimulation to modify stress and initiate small earthquakes. Induced seismicity experiments are ongoing, triggering earthquakes at very low magnitudes (<

0.5). The current set-up of the installed ArtEmis and other sensors within the BULGG niche (Bedretto underground laboratory for geosciences and geoennergies) is shown in Figure 4.2. The ArtEmis sensor was immersed in a tank (IBC) of water that outflowed from one of the monitoring boreholes. Several additional instruments were set-up monitoring various geochemical properties simultaneously as discussed below.

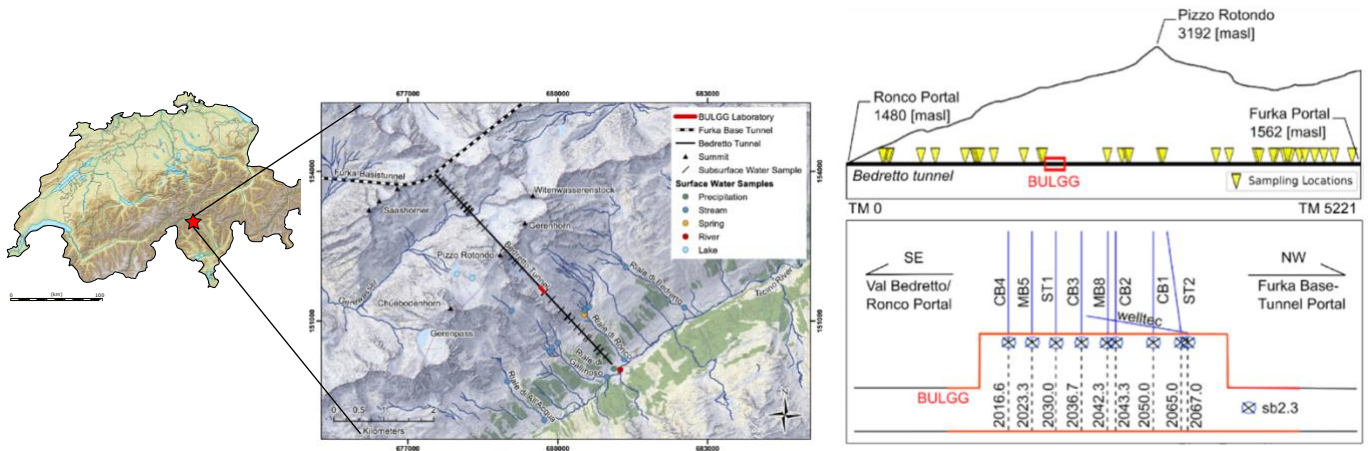


Figure 4.1: Left: Geographical location (red star) of the Bedretto tunnel where induced seismicity is investigated. Centre: Zoom in of the tunnel which extends from the Bedretto Valley to the Furka Basistunnel in canton Ticino. Figure 1b has been adapted from Arnet et al., 2021 Right: Figure 2: Sid profile: indicating the BULGG situation and borehole layout.

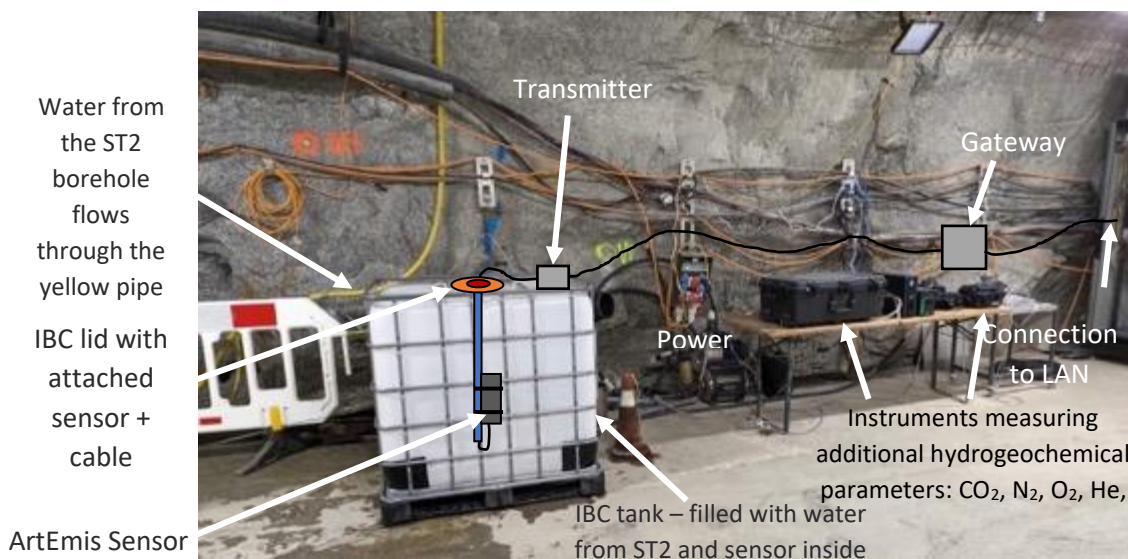


Figure 4.2: Equipment and sensors surrounding the monitoring borehole, ST2, which has water outflow of up to 30L/min. The larger IBC tank contains the ArtEmis sensor. The black box to the right is the miniRuedi aimed at quantifying additional geochemical parameters. Finally, the Rad8 instrument is situated on the far-right end of the table.

#### 4.2 Monitoring and operation of the installed sensors

##### ArtEmis sensor

On 05.03.2024, the ArtEmis sensor was installed in the BULGG section of the Bedretto tunnel. Upon its initial operation, the Radon (Rn) spectrum revealed the presence of gamma emissions from both the thorium and uranium series, which obscured the expected sharp Rn peak at 609 keV (corresponding to a specific channel).

To address this, more advanced electronics will be employed to develop a new detector capable of clearly detecting Radon traces. On the 27.08.2024, it was noted that there was water ingress on one of the ethernet connection cables. The sensor will therefore be sent back for repair and returned to the Bedretto Lab for re-installation.

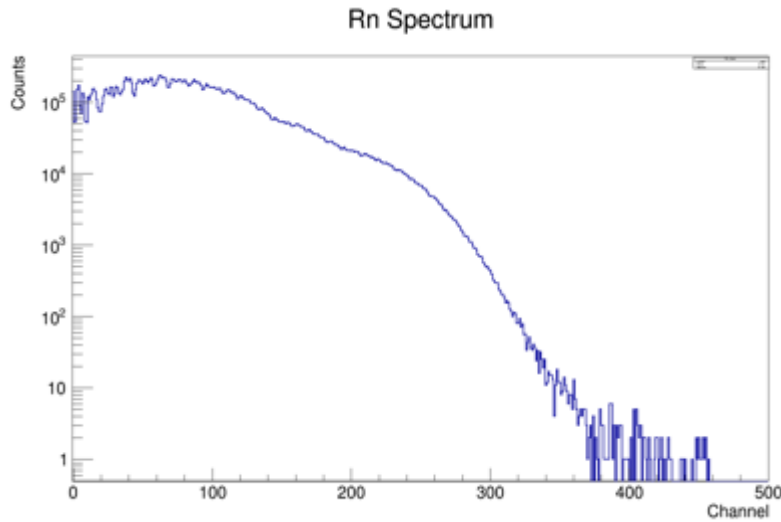


Figure 4.3: Initial spectrum from the ArtEmis sensor detailing the number of counts (related to Rn activity) vs. Channel number (gamma energy).

RAD8 device

The RAD8 is a comparable device that can be applied to measure radon activity in groundwater, though it operates on a fundamentally different principle to the ArtEmis sensor and is not cost effective for the ultimate goals of the ArtEmis project. Further, unlike the ArtEmis sensor, which can be easily submerged in water, the RAD8 requires complex separation of radon (gas) from the water phase before measurement. Despite these differences, the RAD8 provides a useful reference for evaluating the performance of the ArtEmis sensor. Figure 4.4 illustrates the radon activity observed during the induced seismic event in Bedretto. A slight increase in Rn activity was detected just before the main triggered seismic event (see section 4.3 below), followed by a sharp decline in activity. However, the current time series data is limited, and further analysis is ongoing to process the remaining data.

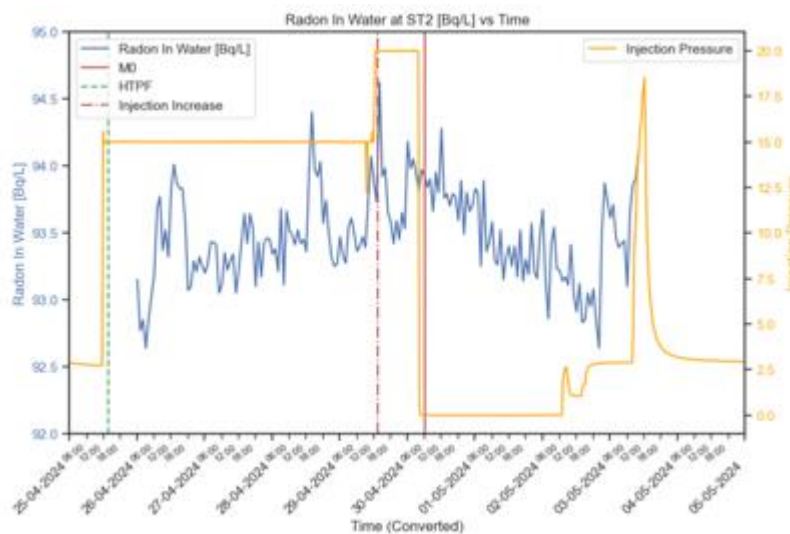


Figure 4.4: Initial spectrum of Rn from the commercial Rad8 device (blue lines). The yellow data line is the water injection pressure (in MPa) at the ST1 borehole (see Section 4.3 for an overview of borehole locations).

### MiniRuedi portable mass spectrometer:

The miniRuedi (Brennwald et al., 2016) continuously measures in water the partial pressures of He, N<sub>2</sub>, O<sub>2</sub>, Ar, CO<sub>2</sub>, and Kr, with the capability to detect additional gases as needed. In addition, total pressure and temperature are measured. Figure 4.5 displays the interface of the device along with the current readings of gases present in the groundwater. The miniRuedi was configured to monitor both dissolved gases in the injection water and in the water emerging from the monitoring borehole, which is believed to be hydrogeologically connected to the injection borehole.

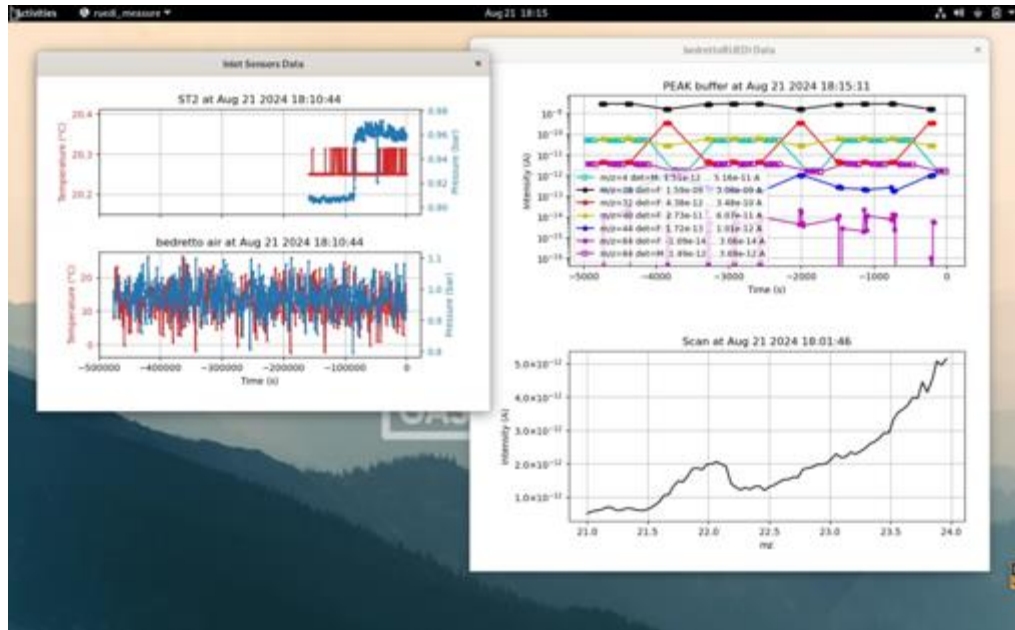


Figure 4.5: MiniRuedi (mass spectrometer) measurements i.e., current readings in Amps of masses: He ( $m=4$ ), N<sub>2</sub> ( $m=28$ ), O<sub>2</sub> ( $m=32$ ), Ar ( $m=40$ ), CO<sub>2</sub> ( $m=44$ ), and Kr ( $m=84$ ), in addition to total pressure and temperature measurements.

### 4.3 Seismicity evolution during the target period

To induce seismicity, a hydrological injection procedure was implemented at the ST1 borehole (see Figures 4.1 & 4.6), supported by remote-controlled software, which allowed the experiment to be conducted outside of the tunnel. The experimental design was to rupture a small volume area in the rock volume, approximately 2x2 m<sup>2</sup>, and ~1cm thick, to investigate the initiation, propagation, and cessation of a micro-earthquake.

On April 30th at 04:09 UTC, the Bedretto seismic network, comprising acoustic sensors, tunnel stations, and surface stations, successfully recorded the first triggered micro-earthquake with a magnitude of -0.4. This event occurred following the injection of approximately 100 m<sup>3</sup> of local groundwater within the tunnel (see Figure 4.4). The earthquake was localized specifically within the targeted Valter volume within BULGG. The precise location of the micro-earthquake, within the context of BULGG, is detailed more specifically in Figure 4.8.

ST1 features an installed packer system, which segments the rock volume along the borehole into discrete sections known as "intervals." Three of these intervals, highlighted in pink in Figure 4.6 and labeled as "Int," were of particular focus during the M0 experiment. Interval 11, chosen for the injection due to its favorable seismicity characteristics and hydraulic isolation (Bröker et al., 2024), was monitored using an array of sensors. These sensors tracked the seismic activity induced during the hydraulic injection within the rock volume

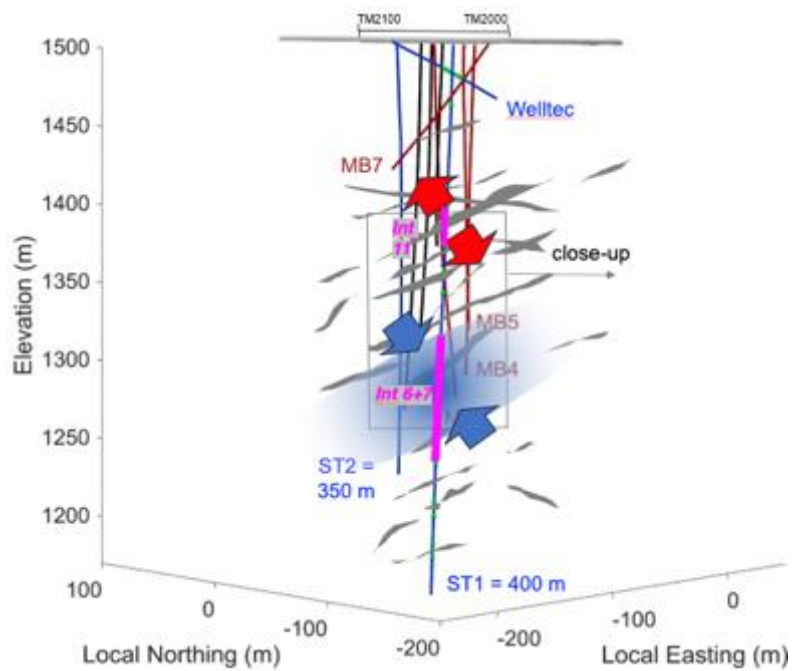


Figure 4.6: ST1 is the hydraulically stimulated borehole and ST2 the monitoring borehole for Rn activity measurements, temperature and other dissolved gas species in the groundwater.

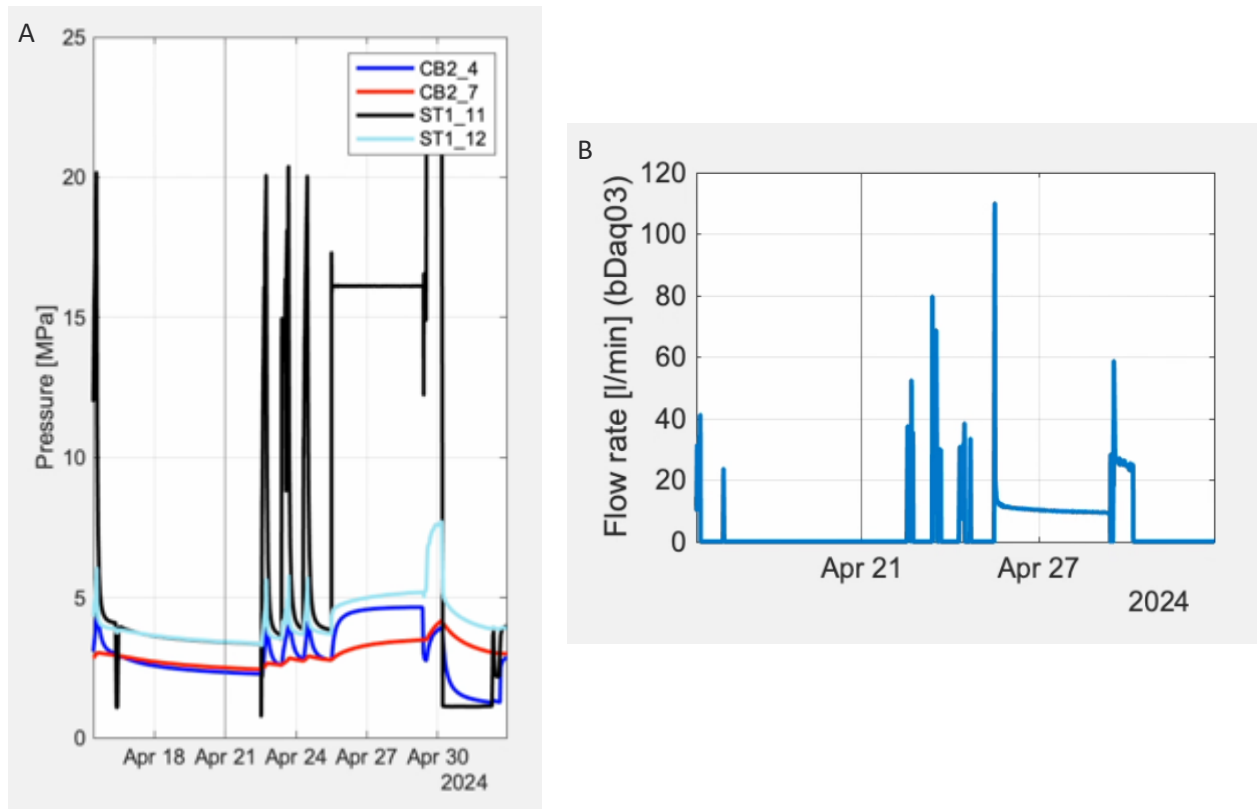


Figure 4.7: A: Injection pressure into ST1 borehole interval 11 over the course of the stimulation. The pressure is also shown for interval 11 (ST1\_11). B: Associated flow rate into the same interval (also see Figure 4.4). “CB2” denotes a Characterisation borehole – testing hydraulic characteristics within the local rock volume.

Figure 4.8 illustrates the spatial distribution of seismic events recorded between April 15, 2024 (09:52), and April 30, 2024 (04:08), with  $b_+$  values mapped onto the events to represent the relative frequency of larger earthquakes (dark red, with  $b_+$  values as low as 1) versus smaller earthquakes (dark gray, with  $b_+$  values up to 1.5). The clustering of  $b_+$  values in specific areas indicates variations in seismic activity and stress distribution. Regions exhibiting lower  $b_+$  values correspond to zones of higher stress accumulation, where the likelihood of larger earthquakes is increased. The yellow star marks the location of the triggered M -0.4 event.

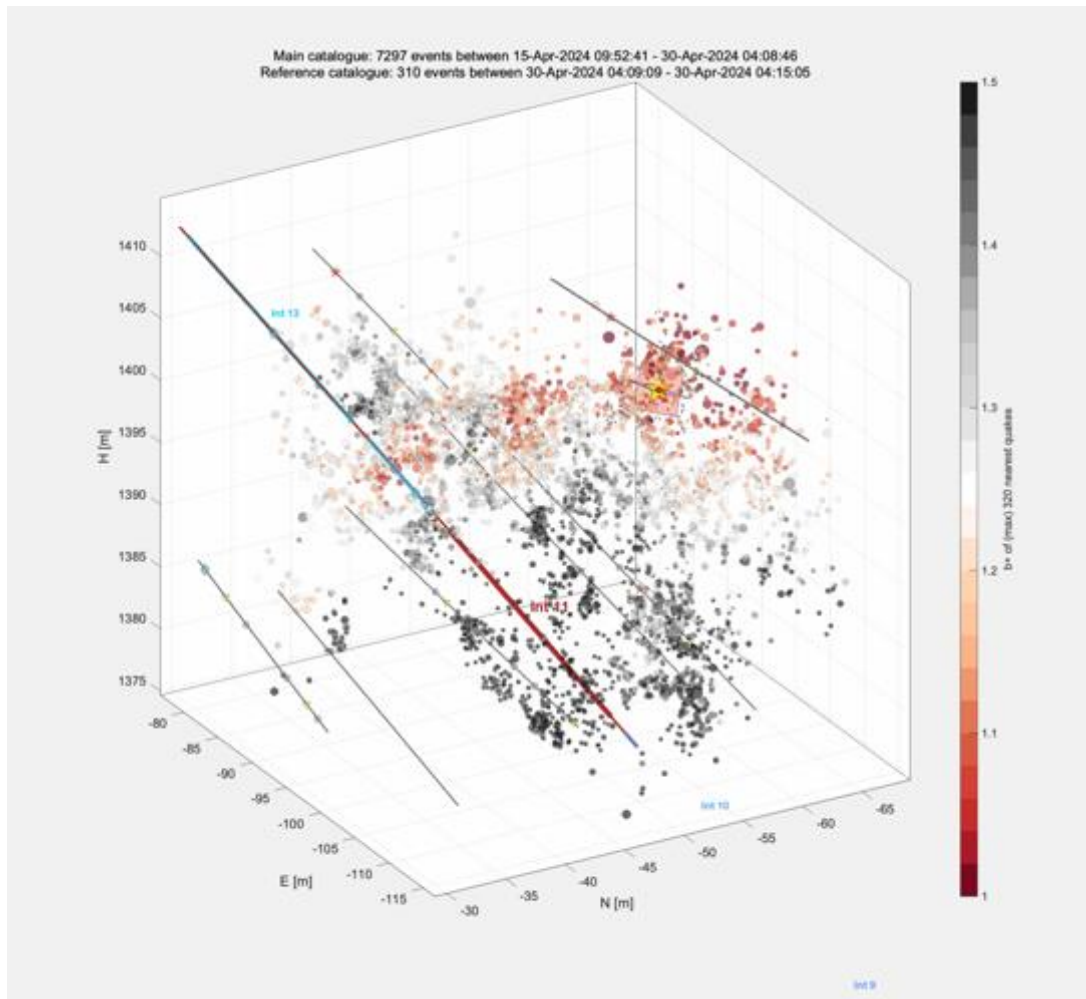


Figure. 4.8: 3D plot showing seismic event data in terms of spatial coordinates: E – Easting, N – Northing, and H – Height. A color-coded  $b_+$  value map events from dark red which is associated with lower  $b_+$  values (large earthquakes are more likely), to dark grey (smaller earthquakes are more likely). The yellow star indicated spatially the location of the -0.4 M induced earthquake.

The successful triggering of this controlled seismic event establishes a framework for future experiments planned under the FEAR project, scheduled to commence in late 2024.

#### 4.4 Geochemical evolution during the target period

Figures 4.9-4.12 show the partial pressures for the specified gas species as measured by the miniRuedi in groundwater from borehole ST2. Notably, the partial pressures of  $N_2$ ,  $CO_2$ , and Ar at the ST2 outflow increased after the onset of the first water injection phase which was conducted at a pressure of 15MPa. However, after three days of continuous water injection at 15MPa, the partial pressures of the gases sharply declined. On 29.04.24 the injection pressure was increased to 20MPa, shortly after which a -0.4M earthquake was triggered. The cause of the sharp decline in gas concentrations remains unclear, and further data analysis

is necessary. One hypothesis suggests that one of the intervals in the characterization boreholes may have closed, potentially affecting water flow, although other physical explanations are also possible.

The changes in observed gas concentrations suggest that during the initial injection phase, water was likely displaced towards ST2, resulting in a different water mixture (or parcel) reaching the ST2 outlet compared to the conditions prior to water injection.

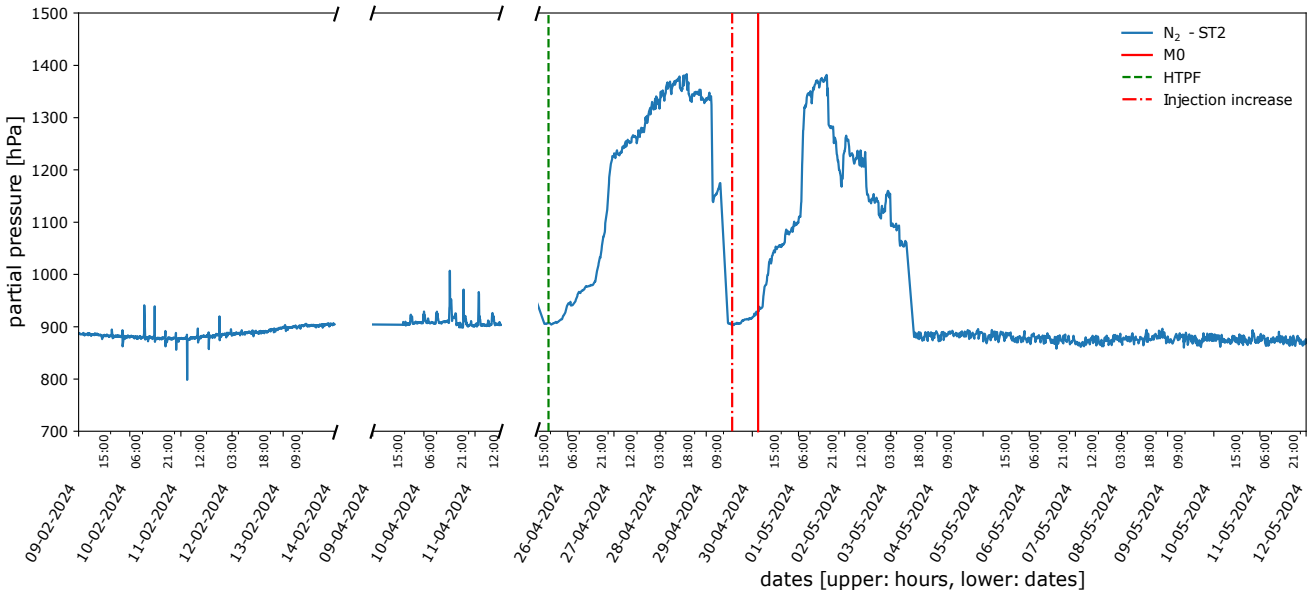


Figure 4.9: N<sub>2</sub> partial pressure in water flowing out of the ST2 borehole vs. time. The solid red line defines the moment of the -0.4 M induced earthquake.

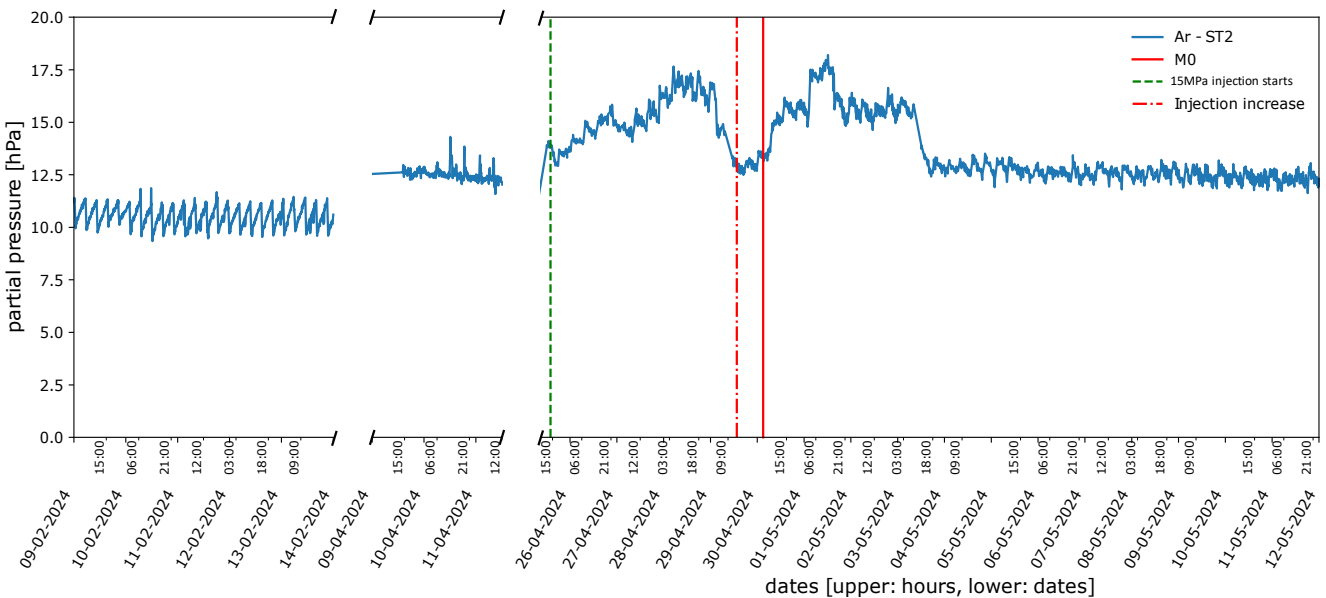


Figure 4.10: Ar partial pressure in water flowing out of the ST2 borehole vs. time, showing similar increase and subsequent decrease in partial pressure as for N<sub>2</sub>.

Figures 4.11 and 4.12 illustrate the partial pressures of Helium and Krypton over time, respectively. While small double peaks are observed in these gases, similar to the other dissolved species, their trends appear slightly distinct, particularly when analyzed as ratios relative to Ar partial pressures (Figures 4.13 and 4.14). The Krypton signature is particularly clear - the injection water was labeled with Kr - allowing us to observe the breakthrough curve for this tracer that seems to follow after the -0.4 M micro-earthquake.

The He/Ar plot suggests that there are additional changes in Helium concentrations relative to the other dissolved gases, potentially related to rock fracturing. Helium naturally emanates from rock into the local pore space and groundwater, and an increase in the rock surface area due to fracturing could lead to more Helium being released into the groundwater locally present. These observations and hypothesis are preliminary, however, and further analysis including comparisons with Radon data, is required for an improved and full understanding of the changes observed during the stimulation.

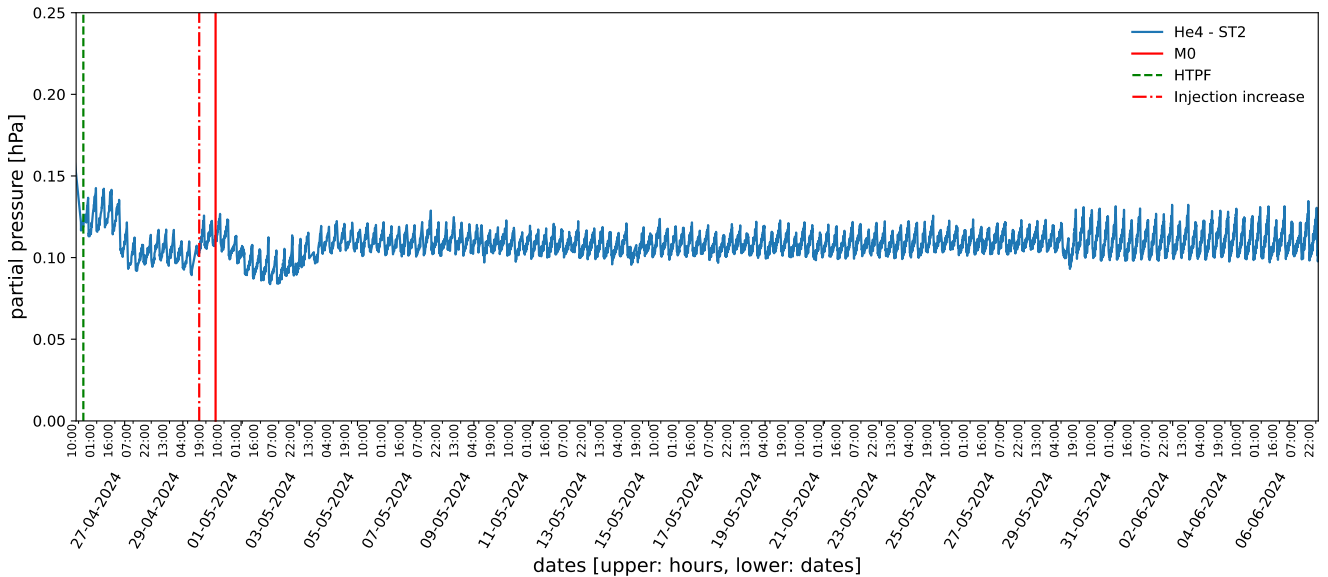


Figure 4.11: Helium (He) partial pressure in water flow out of the ST2 borehole over time. He shows a distinctively different trend to the other dissolved gases (besides Kr). He shows an increase in partial pressure immediately after the hydraulic pressure increase and preceding the induced M0.

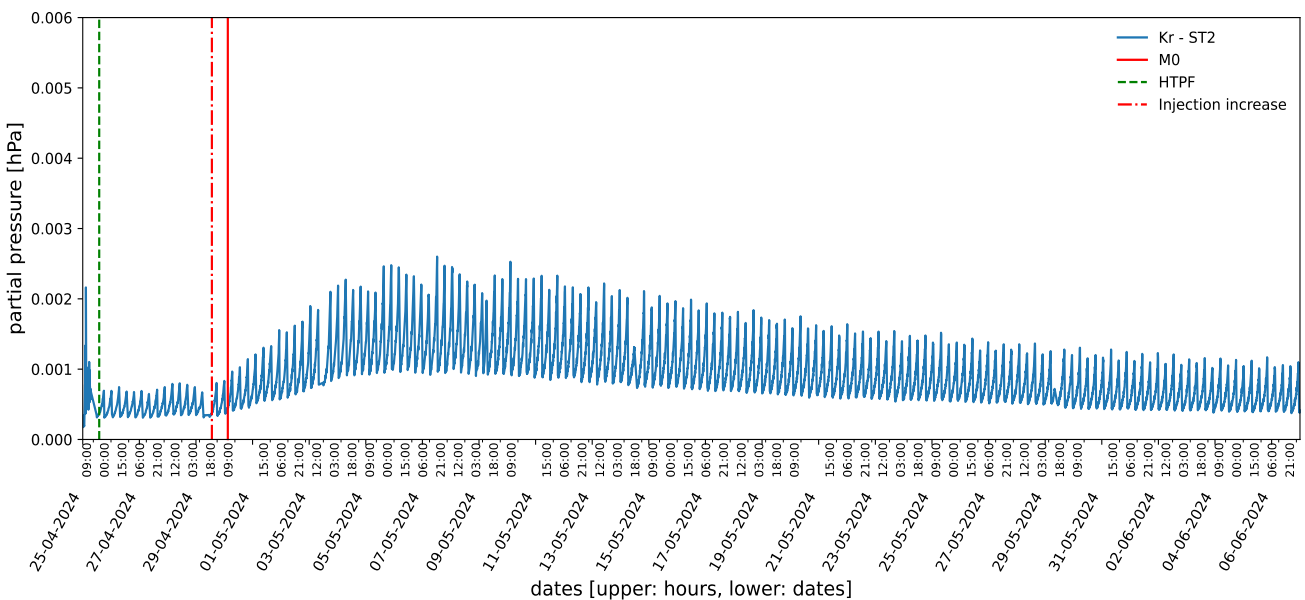


Figure 4.12: Kr partial pressure in water flowing out of the ST2 borehole over time. Kr increase subsequent to the M0 most likely as a result of new fractures created in the rock volume allowing a more transmissive flow path between the ST1 and ST2 boreholes. Ultimately, the breakthrough of Kr is observed from the injection water. Kr was added to the injection water both during 15 MPa and again at the 20 MPa injection pressure. Notably the breakthrough is only observed after the -0.4 M earthquake was stimulated.

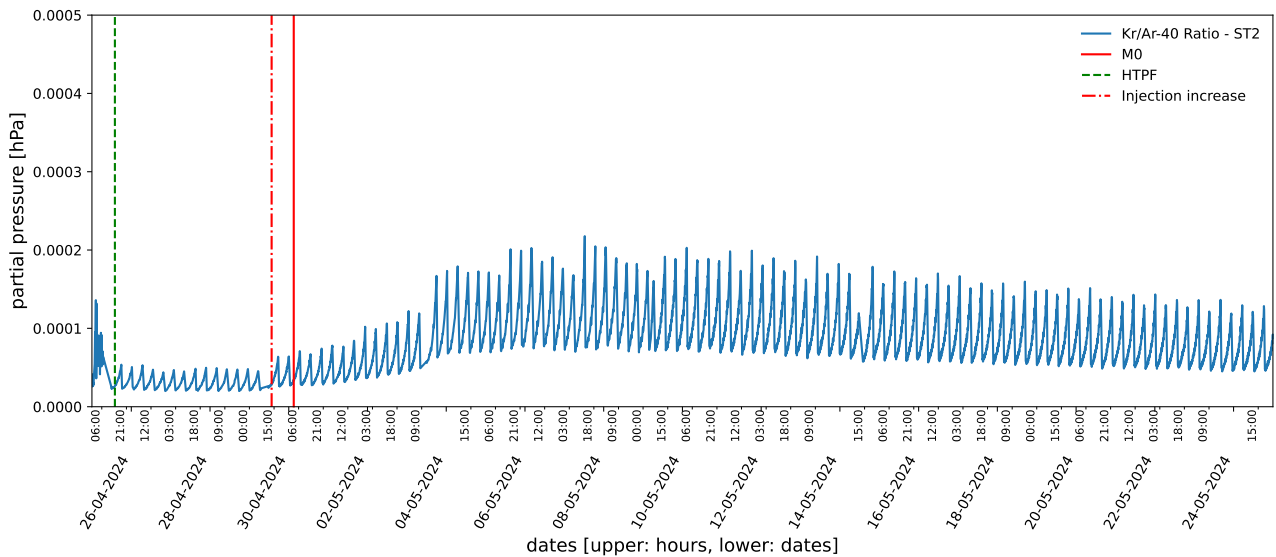


Figure 4.13: Kr/Ar ratio more clearly earmarking the breakthrough of the injected water from ST1 into ST2.

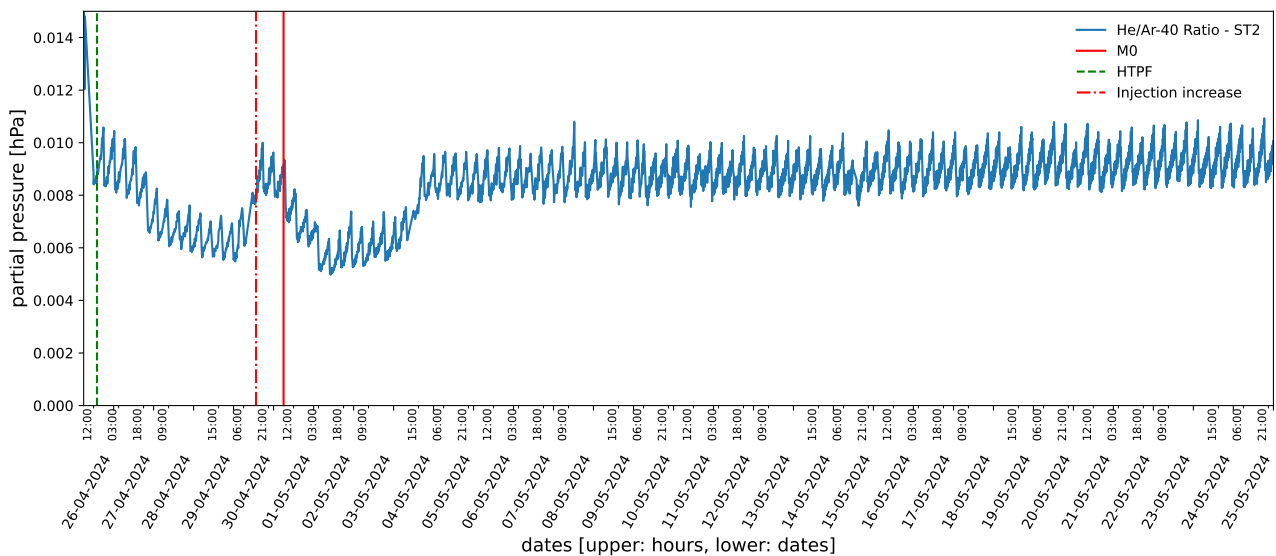


Figure 4.14:  $^4\text{He}/^{40}\text{Ar}$  ratio more clearly identifies the change in He concentrations relative to Ar concentrations. The anticipated He concentration change immediately prior to the injected pressure increase and -0.4 M earthquake could be in response to He emanation into the pore space of the rock volume and subsequent dissolution into the local groundwater.

## 4.5 References

- Arnet, M. 2021. Deep Alpine Fluids: Origin, pathways and dynamic remobilisation in response to hydraulic stimulations at the Bedretto Underground Laboratory for Geosciences and Geoenergies (BULGG). Master's Thesis, ETH Zurich. <https://doi.org/10.3929/ethz-b-000532915>
- Brennwald, M. S., Schmidt, M., Oser, J., Kipfer, R. 2016. A Portable and Autonomous Mass Spectrometric System for On-Site Environmental Gas Analysis. *Environmental Science and Technology* 50(24), 13455-13463. <https://doi.org/10.1021/acs.est.6b03669>
- Bröker, K., Ma X., Doonechaly, N.G., Roskopf, M., Obermann A., Rinaldi, A.P., Hertrich, M., Francisco Serbeto, F., Maurer, H., Wiemer, S., Giardini, D. 2024. Hydromechanical characterization of a fractured crystalline rock volume during multi-stage hydraulic stimulations at the BedrettoLab. *Geothermics* 124, 103126. <https://doi.org/10.1016/j.geothermics.2024.103126>

Keller, F., Schneider, T.R. 1982. *Geologie und Geotechnik*. Schweizer Ingenieur und Architekt 24, 512–520

Ma, X., Hertrich, M., Amann, F., Bröker, K., Gholizadeh Doonechaly, N., Gischig, V., Hochreutener, R., Kästli, P., Krietsch, H., Marti, M., Nägeli, B., Nejati, M., Obermann, A., Plenkers, K., Rinaldi, A. P., Shakas, A., Villiger, L., Wenning, Q., Zappone, A., Bethmann, F., Castilla, R., Seberto, F., Meier, P., Driesner, T., Loew, S., Maurer, H., Saar, M. O., Wiemer, S., Giardini, D. 2022. Multi-disciplinary characterizations of the BedrettoLab – a new underground geoscience research facility. *Solid Earth* 13, 301–322. <https://doi.org/10.5194/se-13-301-2022>

Rast, M., Galli, A., Ruh, J.B., Guillong, M., Madonna, C. 2022. Geology along the Bedretto tunnel: kinematic and geochronological constraints on the evolution of the Gotthard Massif (Central Alps). *Swiss Journal of Geosciences*. 115, 8. <https://doi.org/10.1186/s00015-022-00409-w>

Wiemer, S., Danciu, L., Edwards, B., Marti, M., Fäh, D., Hiemer, S., Wössner, J., Cauzzi, C., Kästli, P., Kremer, K. 2016. Seismic Hazard Model 2015 for Switzerland. 1–163. <https://doi.org/10.12686/a2>

### Websites

FEAR 2024. “Fault Activating and Earthquake Rupture” URL: <http://fear-earthquake-research.org/home> (accessed 26.06.2024).

SED 2024. FDSN Web Services. URL <http://www.seismo.ethz.ch/en/research-and-teaching/products-software/fdsn-web-services/> (accessed 26.08.2024).